Icing Physics Studies Using the 3D SIDRM Test Article: Ice Crystal Icing Analysis

Tadas P. Bartkus[1]
Ohio Aerospace Institute, Cleveland, Ohio, 44142, USA

Sam Lee[2]
HX5, LLC, Cleveland, OH, 44135, USA

In-flight icing is an important safety issue and is a factor that affects aircraft design and performance. Newer regulations are driving a need for improvements in airframe and engine icing simulation capability. Experimental data is required for the development of icing physics models and simulation validation. This paper presents the analysis of the ice crystal icing data subset from tests conducted in 2022 at the NASA Icing Research Tunnel that studied both supercooled liquid and ice-crystal icing. The test article that was utilized replicated 3D geometrical features of an inter-compressor duct and strut region of a turbofan engine. The surfaces of the Simulated Inter-compressor Duct Research Model (SIDRM) can be heated to simulate the warm surfaces of the turbofan inter-compressor duct. The test article is instrumented with pressure taps, heaters, heat flux gauges, and thermocouples, while a 3D laser scanner, cameras, and a weighing scale to measure ice mass were utilized to characterize the icing behavior. The aim of these tests was to generate ice accretions on the SIDRM test article under well-characterized icing conditions. To that end, ice crystal cloud characterization tests were conducted that provided cloud property values at the test section. The ice crystal accretion tests investigated how different test condition parameters impacted ice accretion size, location, and characteristics (such as physical attributes). A key finding was that a sufficiently high surface heat flux at the leading edge can provide a continuous supply of liquid melt to critical accretion zones downstream, resulting in elevated ice mass accretions. Another key finding was that warmer heater settings in critical accretion zones can suppress ice accretion. These findings are consistent with icing behavior observed in full-scale engine icing tests conducted previously at the NASA Glenn Research Center. Test runs investigating the contribution of liquid melt generated at the leading edge found that the melt can be transported downstream to critical accretion regions in two forms, via runback and splash. The form of melt supplied downstream affected accretion behavior and features. Sharkteeth-shaped ice accretions were generated at certain test conditions, a physical attribute that has been observed in full-scale engine icing tests. The ice accretion data will be used to develop and validate 3D computational engine icing tools, such as GlennICE, that predictively assesses the onset and growth of ice. One of the goals of the sponsoring NASA project is to develop simulation models and tools that can assist in the design and certification of engines for flight in icing conditions in a cost-effective way.

I. Nomenclature

AOA	=	angle of attack (angle in degrees)
IWC	=	ice water content (g/m^3)
MVD	=	median volumetric diameter (µm)
$P_{air,noz}$	=	spray bar nozzle atomizing air pressure (psig)

[1] Senior Researcher, NASA GRC Icing Branch, 21000 Brookpark Rd., MS 11-1, AIAA Senior Member.
[2] Engineer V, NASA GRC Icing Branch, 21000 Brookpark Rd., MS 11-2, AIAA Senior Member.

$P_{delta,noz}$	=	spray bar nozzle water pressure differential, water pressure minus atomizing air pressure (psid)
t	=	time (s)
T_0	=	total air temperature (°C)
$T_{air,noz}$	=	spray bar nozzle atomizing air temperature (°C)
$T_{water,noz}$	=	spray bar nozzle water temperature (°C)
TWC	=	total water content, liquid water content plus ice water content (g/m^3)
U	=	tunnel airspeed (knots)
$\beta_{collision}$	=	collision efficiency, the fraction of particles within a stream tube that collides with a surface (non-dim)
$\beta_{collection}$	=	collection efficiency, the fraction of particles within a stream tube that collects on a surface (non-dim)

II. Introduction

Numerous reports of turbofan engine power-loss or damage events have been attributed to the ingestion of ice crystals [1,2]. These events typically occur in deep convective updraft systems and have included engine stall, rollback, flameout, surge, and engine component damage. Mason et al. [3] hypothesized that ice crystals ingested into the engine undergo partial melting within the warm compressor system and then, as a mixed-phase water mass, accrete on surfaces within the engine core. Stressing the importance of mitigating this threat posed by engine icing, the Federal Aviation Administration (FAA) released a document outlining existing ice crystal icing research needs [4]. Research efforts in understanding the physics of ice crystal icing have grown to address this flight safety threat. Numerous component level tests utilizing static airfoils have been conducted investigating the fundamental ice crystal icing physics [5-17]. More complex ice crystal accretion studies utilized heated ducts [18-19]. More recently, the National Research Council of Canada commissioned the Ice Crystal Environment Modular Axial Compressor Rig (ICE-MACR) to simulate turbofan compressor physics more closely [20-23]. With rotating machinery, the sub-scale rig allows for studies of fundamental physics such as centrifuging, particle breakup, annular accretion, and particle melt due to compression and conductive heating.

The National Aeronautics and Space Administration (NASA) Glenn Research Center has conducted several experiments to better understand ice crystal icing. Multiple full-scale engine icing tests have been conducted at the NASA Propulsion Systems Laboratory (PSL) [24-34]. Of note was the engine icing test entry utilizing the heavily instrumented, unmodified Honeywell ALF502R-5 engine, serial number LF11.Tests were successful in replicating known engine rollback test conditions, indicating reliable simulation of flight conditions and engine performance in a ground facility. Several key findings related to surface heating were provided. Testing data showed that the addition of upstream heat sources from the spinner heat and inlet guide vane anti-ice system promoted ice accretion and rollback. In addition, increasing the fan speed raised the temperature in the core flowpath suppressing accretion, avoiding engine rollback. Video that was made publicly available [30] showed ice accretion aft of the exit guide vane with sharkteeth-shaped ice features that drew interest from the engine icing community.

The full-scale engine icing tests provided valuable information replicating realistic flight conditions. Due to the inaccessibility to the test section and internal compartments of the engine, much of the ice accretion data is qualitative in nature. Quantitative measurements of ice mass and accretion geometry, including surface heat flux was not measured or possible. Quantitative data are needed to properly predict the onset and growth of ice within turbofan engines from first principles. To that end, NASA has conducted a series of component level tests to study the fundamental ice crystal accretion physics [5-6, 8-9, 35-38], supplementing what was learned in the full-scale engine icing tests. The first two test entries in this series of accretion physics studies were conducted in the NASA PSL in 2016 [8-9] and 2018 [5-6]. These tests generated a dataset of ice accretions on an unheated NACA 0012 airfoil with a focus on the cloud melt ratio impact on ice accretion. Quantitative ice geometry measurements were limited to extracting 1D and 2D ice shapes from orthogonal video images that captured the ice growth at the NACA 0012 leading edge.

NASA conducted the next test in the series of component level icing physics tests at the NASA Icing Research Tunnel (IRT) [35-38]. The results reported in this paper are from the icing tests conducted in 2022. The ice accretion tests utilized the Simulated Inter-compressor Duct Research Model (SIDRM), a 3D test article whose geometry is representative of an inter-compressor duct and strut region of a turbofan engine. The test article has the ability to heat its surfaces to simulate the warm surfaces of the turbofan inter-compressor duct, and is instrumented with heaters, heat flux gauges, thermocouples, and pressure taps. It should be noted that these tests do not fully simulate the environment within the engine. The testing air temperatures were below freezing, and the icing clouds were fully glaciated before making impact with the test article surface. It is believed that ingested ice crystal clouds are partially melted as they pass through warm engine passages before impacting internal engine components. In addition, this open geometry will result in different pressures and flow compared to the ducted region of the compressor. Despite these limitations, the data collected provide quantitative measurements useful for better understanding of the fundamental ice crystal icing physics.

The aim of these tests was to generate ice accretions on the SIDRM test article under well-characterized conditions. Icing tests were conducted under ice crystal icing and supercooled water icing conditions for this test entry. Results from the supercooled liquid icing subset have been previously presented [35]. The supercooled liquid icing tests provided simulation validation data on a 3D geometry. In addition, an estimate of collection efficiency was back-calculated from ice accretion geometry which is also required for ice crystal icing simulation [36]. This paper focuses on the analysis of the ice crystal icing data subset. The IRT is well calibrated for supercooled water icing, but not for ice crystal icing clouds. To that end, ice crystal cloud characterization tests were conducted to provide proper icing cloud condition values for the ice crystal accretion tests, with results discussed in this paper. The icing physics data measured during the ice accretion tests will be used to develop and validate engine icing computational tools [39-51] such as the 3D simulation tool GlennICE [39-48]. These testing efforts are part of NASA's Advanced Air Transport Technology (AATT) Project activities to improve understanding of the ice growth physics and advance engine aero thermodynamic modeling tools to predictively assess the onset and growth of ice in current and future engines during flight. Simulation tools like GlennICE will allow industry to design and certify engines for flight in icing conditions in a cost-effective way.

III. Ice Crystal Cloud Characterization Tests at IRT

The IRT was built for the primary purpose of conducting icing tests utilizing a supercooled liquid icing cloud. In recent years, efforts have investigated the generation of ice crystal clouds in the icing wind tunnel. Deionized liquid water is ejected from the spray bars, and with a sufficiently cold environment, the cloud freezes as convective heat transfer and evaporative cooling extract heat from the drops. Glaciation is more likely to occur with colder tunnel air temperatures, smaller drop sizes, and colder spray bar settings. It is necessary to know the cloud conditions at the test section to properly assess the resulting ice crystal accretion utilizing the SIDRM test article. A comprehensive ice crystal cloud characterization was conducted that quantified ice water content (*IWC*), cloud particle size distribution (PSD), air temperature and humidity. The following subsections provide highlights from the ice crystal cloud characterization tests conducted to complement the ice crystal accretion tests.

A. Instruments and Test Configurations

A multiweek effort was dedicated to characterizing the air and ice crystal cloud at the IRT test section. There were six configurations of instrumentation utilized during these tests (Fig. 1) and are described below. A list of the instruments with abbreviations and measurement capabilities is provide in Table 1. All instruments were stationary point measurements except for the centerline Multiwire instrument in Configuration 6 which was traversed vertically.

- Configuration 1 utilized two Multiwire probes (MW) developed by Scientific Engineering Associates, an Ice Detector probe (ID) developed by UTC Aerospace, and a Background Humidity Bent Tube probe (BHBT) that was built in-house. The two MWs were used to determine if the sprayed clouds were glaciated and provided information on spatial uniformity of the cloud. The ID provided additional information if a cloud was fully glaciated. The rearward facing BHBT sipped air and measured humidity content using LI-COR and Spectrasensor instruments. Configuration 1 identified 12 conditions with glaciated clouds that measured spatially uniform between the two MW probe locations.
- Configuration 2 swapped out the centerline MW for the Isokinetic Probe version 2 (IKP2), which was used to measure the cloud total water content (*TWC*), or in a fully glaciated cloud, the ice water content.
- Configuration 3 swapped out the ID for the Total Air Temperature probe (TAT) developed by Rosemount and had a Rearward Facing Probe (RFP) that was built inhouse. Both new instruments in Configuration 3 measured total air temperature. In addition, the RFP measured humidity with LI-COR and Spectrasensor instruments.
- Configuration 4 had only the Particle Imaging Ice Crystal probe (PI-IC) installed at the centerline. Developed by Artium LLC, the instrument measured cloud particle size distribution.
- Configuration 5 had only the MW installed at the centerline, where icing sprays were run for longer durations to better quantify cloud recirculation effects and its impact on *IWC* with respect to spray time.
- Configuration 6 had two MW installed, where the centerline MW was mounted on a vertically traversing stand. These tests provided information on *IWC* spatial uniformity, with a focus on the vertical +/-12" space at the center of the test section.

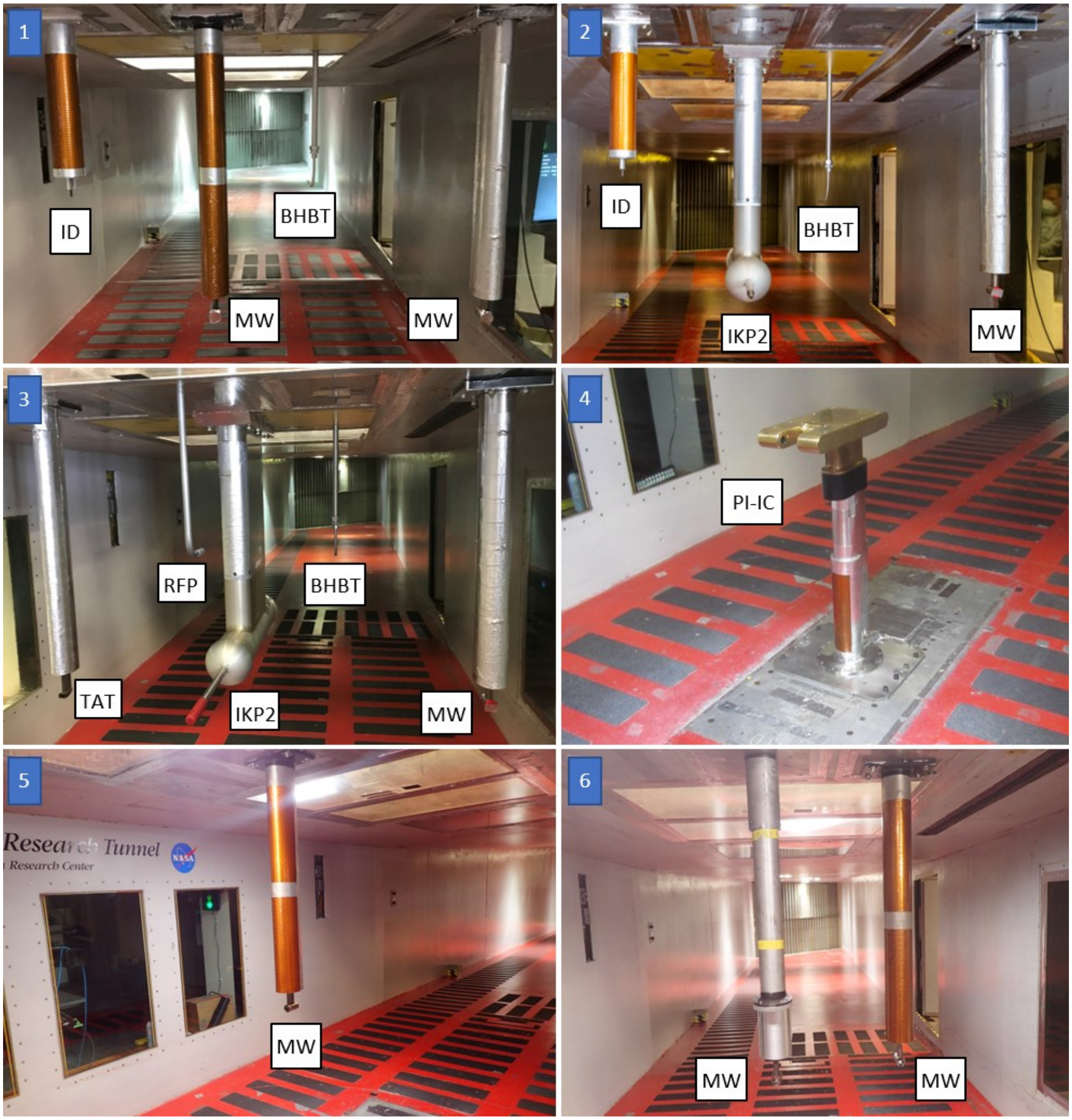

Fig. 1 Instrument Configurations 1 – 6 in the IRT test section utilized to characterize the generated ice crystal cloud.

Table 1 Instruments used to characterize ice crystal clouds in the IRT test section.

Test Section Instrument	Measurement
MW - Multiwire probe (SEA)	Melt ratio and recirculation
IKP2 - Isokinetic Probe Version 2 (SEA)	Total water content and recirculation
RFP - Rearward Facing Probe (in-house)	Air temperature and humidity
PI-IC - Particle Imaging - Ice Crystal probe (Artium)	Particle size distribution
TAT – Total Air Temperature probe (Rosemount)	Air temperature
ID - Ice Detector probe (UTC Aerospace)	Glaciation (liquid presence)
BHBT - Background Humidity Bent Tube probe (in-house)	Humidity

There were 12 ice crystal test conditions that were identified from Configuration 1 for full characterization. These 12 conditions are listed in Table 2 and were selected because they measured as fully glaciated and spatially uniform according to the two Multiwire probes in Configuration 1. Table 2 provides the resulting median volumetric diameter (*MVD)* and *IWC* at the test section for the given spray nozzle and tunnel settings. The 12 conditions are identified by a Spray ID number, listed in the first column of Table 2.

Table 2 Key values listed for the 12 ice crystal cloud conditions that were fully characterized.

Spray ID	$T_{air,noz}$	$T_{water,noz}$	$P_{air,noz}$	$P_{delta,noz}$	T_0	*U*	*MVD*	*IWC*
Letter#	°C	°C	psig	psid	°C	knots	µm	g/m^3
C11	22.5	42.5	60	230	-15	150	26.6	1.93
D11	22.5	42.5	60	230	-15	200	27.9	1.98
E11	22.5	42.5	60	230	-15	250	30.2	2.14
H3	32.5	42.5	60	230	-20	150	26.3	2.16
H9	22.5	42.5	40	175	-20	150	31.6	2.28
H10	22.5	42.5	40	250	-20	150	40.8	3.03
I3	32.5	42.5	60	230	-20	200	28.8	2.00
I9	22.5	42.5	40	175	-20	200	34.9	2.20
I10	22.5	42.5	40	250	-20	200	42.1	3.32
J3	32.5	42.5	60	230	-20	250	30.6	2.20
J9	22.5	42.5	40	175	-20	250	36.3	2.33
J10	22.5	42.5	40	250	-20	250	43.6	3.48

B. Ice Crystal Cloud Generation

The IRT generates an icing cloud utilizing an array of spray nozzles set within 10 spray bars in the wind tunnel. A co-flow of water and atomizing air are used to generate plumes of water droplets. Standard operating procedures to produce a supercooled liquid icing cloud is to set the water and atomizing air temperature within the spray bar system between 80 to 85 °C, which was determined for proper supercooling of the drops as they reach the test section and to prevent the spray nozzles from freezing. Through evaporative cooling and convective heat transfer, the liquid drops decrease to supercooled temperatures as they reach the test section. To generate an ice crystal cloud utilizing deionized water, spray bar water temperature ($T_{water,noz}$) and atomizing air temperatures ($T_{air,noz}$) are set lower ($T_{water,noz}$ = 42.5 °C and $T_{air,noz}$ = 22.5 or 32.5 °C). This reduces the amount of sensible heat that needs to be removed to get to supercooled temperatures. However, to glaciate the liquid drops, nucleation must occur. This can be achieved by driving the temperature colder, and/or potentially disturb the drops from the shocks that result from the under-expanded pressurized nozzle air. Higher nozzle pressures result in stronger shocks locally around the nozzle spray plume, which also results in smaller droplets as the stream of water experiences greater atomization. Smaller drops decrease in temperature more readily than larger drops, promoting drop freezeout. The expanded nozzle air also results in a low static temperature locally around the nozzle plume, which may aid the glaciation process.

Nozzle water and air temperatures were reduced to aid drop freezeout but remained sufficiently warm to avoid nozzles freezing. These efforts were necessary as a single frozen nozzle can affect *IWC* as well as cloud uniformity, which is particularly important if the nozzle correlates to a space near the centerline in the test section.

C. Ice Crystal Cloud Recirculation

The IRT is a closed-loop facility. When spraying supercooled liquid clouds, all the droplets eventually contact a surface, either in the test section or further downstream (such as on turning vanes or heat exchanger) and freeze on the surface upon impact. Thus, all of the cloud is removed from the airflow before it has a chance to recirculate. The only water content in the test section is that directly ejected from the spray nozzles. However, ice crystal particles do not necessarily stick to the surface upon impact, and ice crystal clouds were observed to recirculate in the IRT. Fig. 2 shows a qualitative example of the recirculation. The figure shows images of the spray bars looking downstream towards the test section, where panel A shows the spray at the initial moments after spray activation and panel B shows the spray with the recirculated ice crystal cloud (indicated by overall opaqueness) visible in the image about 20 seconds later. The recirculating of ice crystal clouds is not unique as the National Research Council of Canada has measured and reported recirculation the at the closed-loop Altitude Icing Wind Tunnel [52, 53].

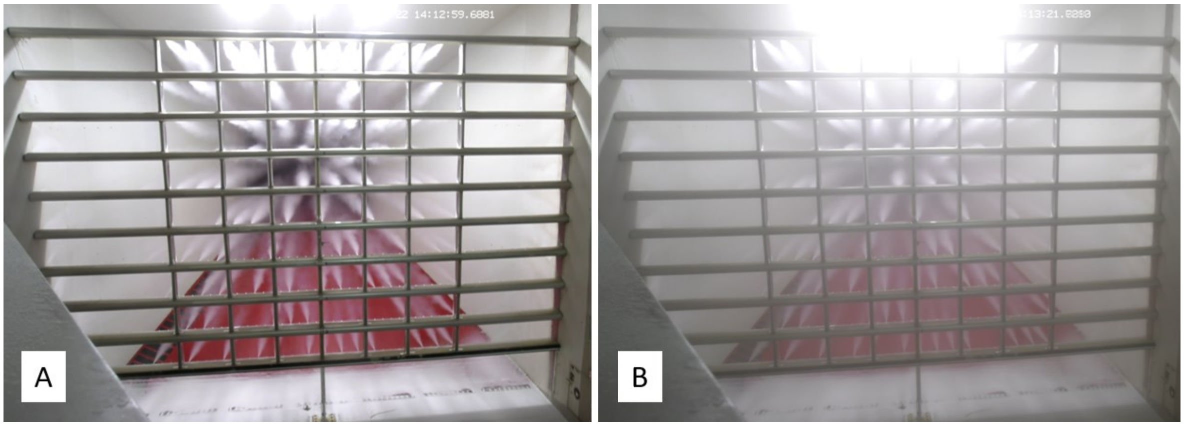

Fig. 2 Images of the spray bars, forward-looking-aft, where panel A shows the spray at the initial moments after spray activation and panel B shows the spray with the visible recirculated ice crystal cloud about 20 seconds later.

Ice water content measurements with the IKP and MW showed the impact of the recirculated cloud, where Multiwire measurements are described and presented in this sub-section to illustrate cloud recirculation. The Multiwire is equipped with three primary hotwires of different sizes and shapes that are used to measure water content [54]. The 083-wire (0.083 in dia) and 021-wire (0.021 in dia) are cylindrical, while the half-pipe (0.083 in dia) is a forward facing half cylinder scoop. In fully liquid clouds, all 3 wires measure approximately the same, but the half-pipe typically measures slightly higher values due to greater collection and retention of droplets striking the hotwire element. In fully glaciated ice crystal clouds, the 021-wire and 083-wire measure near zero values as ice particles largely bounce off, whereas as the half-pipe will capture a significant fraction of the impinging ice crystal cloud. Multiwire 083-wire readings that measured less than 8% of half-pipe values, also referred to as false response, were considered fully glaciated clouds during testing. Larger false response values were determined to represent mixed-phase clouds.

Figure 3 shows the measurement of the centerline Multiwire half-pipe (MW_HP) and 083-wire (MW_083) with respect to time as measured during Configuration 6 and is typical of all 12 ice crystal test conditions. While the true *IWC* value is about 40% greater than what is shown (due to ice crystal retention efficiency of the half pipe), the half pipe reading acts as a proxy for Ice Water Content. For this illustrative purpose the focus is on the measurement trend. The icing cloud is activated at time $t = 0$ s. The measurement for the first 20 seconds (denoted by A) relates to the *IWC* contribution from the spray nozzles only and is flat for that short period. For the time interval from about $t = 20$ to 60 s (denoted by B), the contribution from the recirculating ice crystal cloud can be seen as it rises steadily until the measurement reaches a near steady value for the remainder of the spray (denoted by C). The measurement appears to be steady for the time segment marked as C, but longer spray durations measured a slow increase during the spray. The values decrease as the spray is turned off, but readings do not fall off to zero immediately as the recirculating cloud continues to flow around the closed-loop tunnel for several seconds longer (denoted by D) until the cloud particles settle out completely.

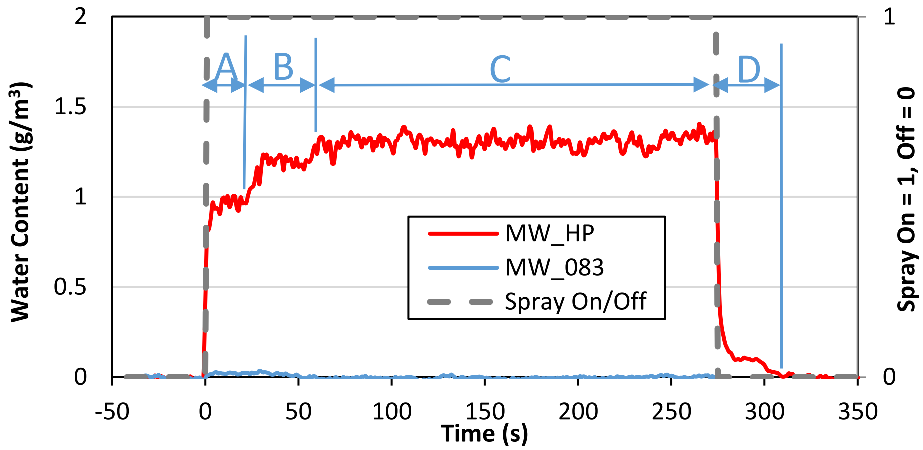

Fig. 3 Measurement of the Multiwire half-pipe at the test section centerline indicating an increase in water content after spray activation due to cloud recirculation.

Figure 4 shows the centerline Multiwire measurements with respect to time from Configuration 5 for an extended duration spray. The half-pipe measurement shows that *IWC* increases with respect to time for long duration sprays. This slow rise is in addition to the more rapid increase observed in the first minute after spray activation due to recirculation. The measurements suggest an accumulating effect from the recirculating ice crystal cloud.

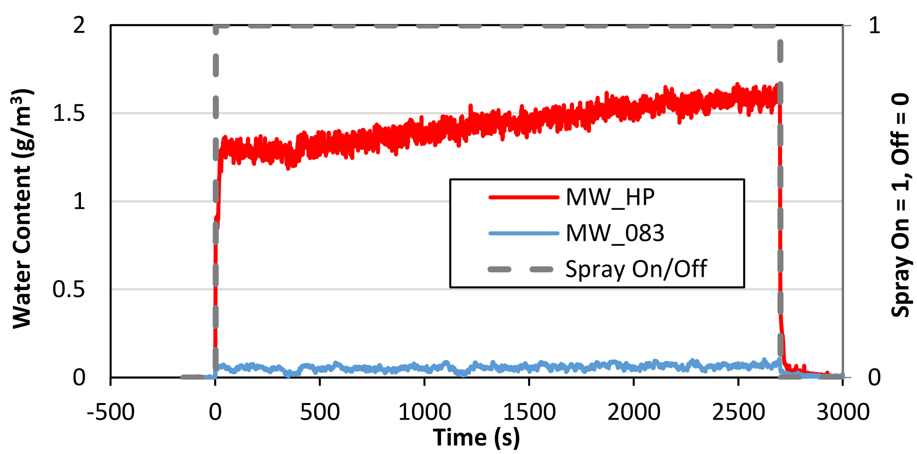

Fig. 4 Measurement of the Multiwire half-pipe at the test section centerline indicating an increase in water content throughout the duration of a longer spray.

The ice crystal particles accumulate on various surfaces throughout the tunnel, including the floors, turning vanes, and heat exchanger fins. It is hypothesized that the ice crystals are loosely adhered to these surfaces and can be kicked back into the circulating cloud even after settling out after the spray is turned off. Figure 5 shows centerline Multiwire measurement with respect to time from Configuration 5 after the spray has been cycled two times. The half-pipe measurement during the first spray shows the slow increase in water content during the long duration spray. The spray was turned off for several minutes for the re-circulating cloud to settle out. Shortly after the second spray activation, water content as measured by the half-pipe element returned to water content values as measured towards the end of the first long spray.

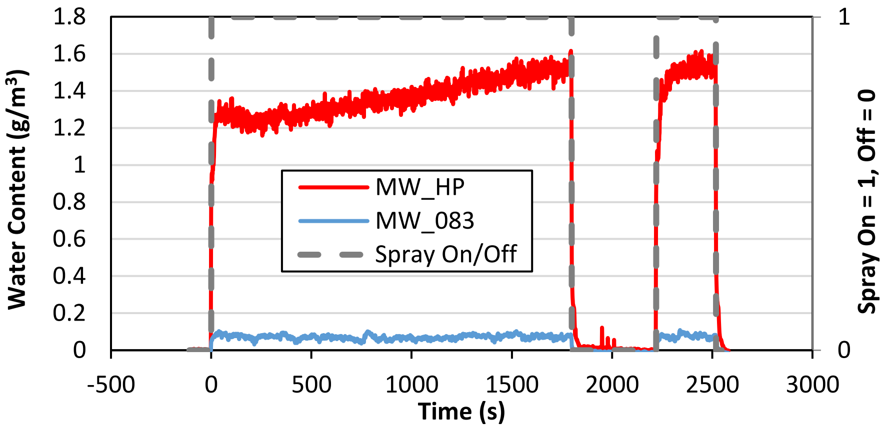

Fig. 5 Measurement of the Multiwire half-pipe at the test section centerline indicating that the accumulated ice crystals on the tunnel surfaces from the initial spray contribute to the overall cloud in the second spray even after several minutes between sprays.

The persistence of ever-increasing water contents due to cloud recirculation (accumulation) required necessary action to produce repeatable and controlled clouds. A full wind tunnel thaw was implemented after 20 minutes of cumulative spray to reset the tunnel. Tunnel air temperature was increased to 10 °C until all surfaces with accumulated ice particles had melted. The procedure took about 45-60 minutes to perform. Figure 6 shows Multiwire half-pipe measurement with respect to time from Configuration 5 for identical spray conditions before and after the thaw procedure. Values are in good agreement and show the effectiveness of the thaw procedure to repeat ice crystal clouds.

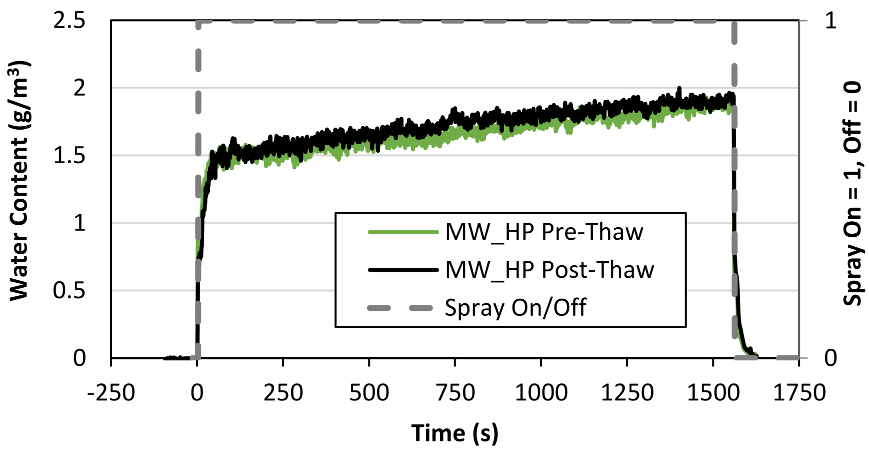

Fig. 6 Measurement of the Multiwire half-pipe at the test section centerline before and after conducting the thaw procedure.

The *IWC* and *MVD* values listed in Table 2 are averaged values from multiple 4-minute test runs where the cumulative spray time was limited 20 minutes. Similarly, ice accretion tests conducted with the SIDRM test article were also limited to 20 minutes of cumulative spray time. A full tunnel thaw procedure was implemented when 20 minutes of spray time was reached to ensure repeatable conditions as produced during the ice crystal cloud characterization tests.

D. Cloud Spatial Uniformity

Due to the newly added variable of cloud recirculation, determining its impact on cloud uniformity at the test section was critical. One of the criteria that was used to identify the 12 test conditions for full characterization was the uniformity measurements between the two Multiwire probes in Configuration 1 as shown in Fig. 1A. These two probes measured at the test section center height of 36 in (91.4 cm) and provided information on the horizontal spatial uniformity. It should be noted that the cloud between the two Multiwires was not necessarily uniform for these 12 test conditions as these were just two point measurements, but the criteria eliminated those conditions that did not measure uniformly between the two spatial locations. The Multiwire measurements from Configuration 6 provided more information on the vertical spatial uniformity from the center of the test section. Figure 5 shows the results from five cloud conditions. The center Multiwire was traversed vertically ±12 in (±30.5 cm) from the centerline. Due to continuous cloud recirculation the lateral Multiwire (stationary) was used as a reference measurement to account for the increasing *TWC* with respect to time. All five cloud conditions in Fig. 7 show similar trends in that greater *IWC* measurements were made towards the floor. This suggests that a larger fraction of the recirculating cloud remained closer to the wind tunnel floor as it passed through the test section, presumably a gravity effect. This vertical variation is important to note for the SIDRM icing tests that focus on measurements over the ±5 in (±12.7 cm) vertical span from the centerline, indicating about ±5% in *IWC* over that vertical range.

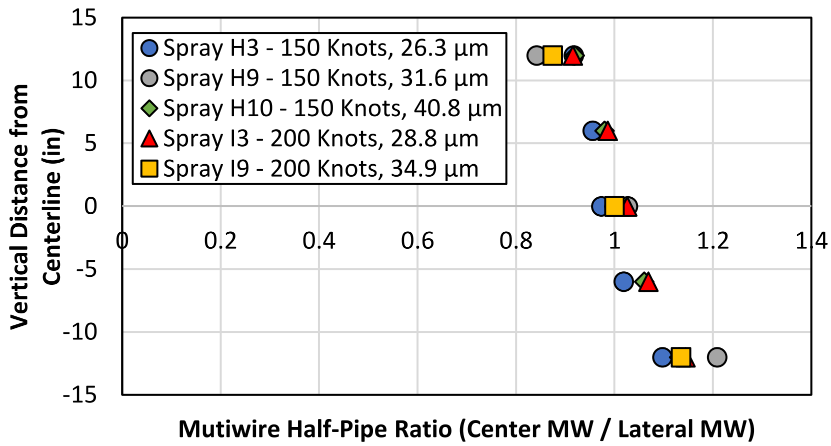

Fig. 7 Multiwire half-pipe ratios between the vertically traversing center Multiwire and the reference lateral Multiwire indicating some vertical non-uniformity, with greater water content below the centerline as compared to above.

IV. SIDRM Test Article

A limited description of the experimental set-up is provided here. For the interested reader, a more detailed description is provided by Bartkus et al. [37] elsewhere. The icing test entry utilized the SIDRM test article, whose schematic with overall dimensions is shown in Fig. 8A. The test article replicates 3D geometrical features of an inter-compressor duct and strut region of a turbofan engine and is highlighted with the red "T" in the circled regions of Fig. 8B and 8C. The middle span (light gray in Fig. 8A) is outfitted with heaters under the aluminum skin allowing it to simulate the warm surfaces of the turbofan inter-compressor duct. The middle span is instrumented with multiple heat flux gauges located between the aluminum skin and film heaters, and surface mounted thermocouples.

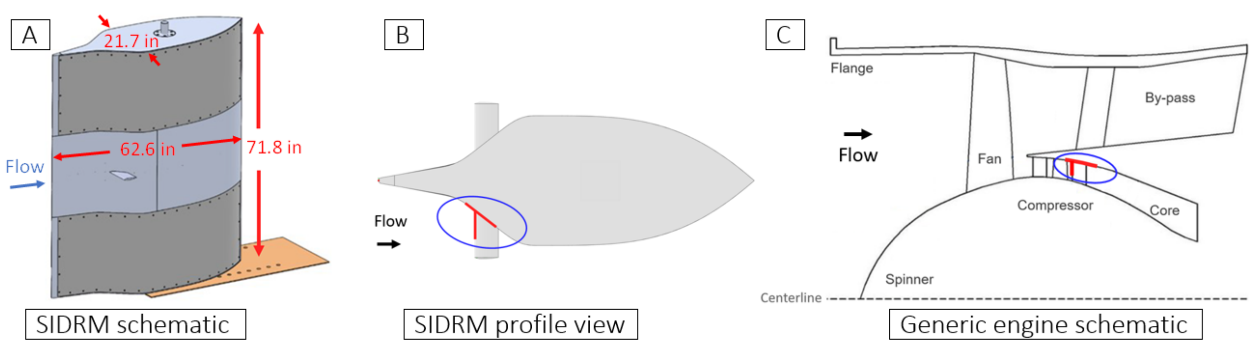

Fig. 8 Schematics of (A) the SIDRM test article, (B) the SIDRM side profile view with a focus on the strut main body junction, and (C) a generic turbofan engine schematic with a highlight showing how the test article geometry relates to the inter-compressor duct and strut region of a turbofan engine.

Figure 9 shows an image of the instrumented side of the SIDRM test article with an overlay of the heater zones approximating the locations they heated. A cartridge heater is located at the test article leading edge (Zone 1), and thin film heaters line the inner mold line along the rest of the chord (Zones 2 through 6). Thin film heaters mirror the non-instrumented side of the test article to maintain symmetry. The heaters span 24 inches and axial lengths covered by the heaters is shown in Fig. 9 (the heater footprint is larger due to surface curvature). Heater Zone 6 is not shown in this image, but covers 14.5 inches aft of Zone 5, with 3.2 inches near the trailing edge unheated for structure fastening purposes. Similarly, the 1.1 inch gap between heater Zones 4 and 5 exists for structure fastening purposes as well. The names and locations of several surface mounted thermocouples are shown indicating in which zone they are located (Not shown is T315 in Zone 6). Additional details of thermocouple locations are provided in Table A-1 in the Appendix. A description of the test article curvature is shown to provide context in the figure, as some of the language will be used later in this paper.

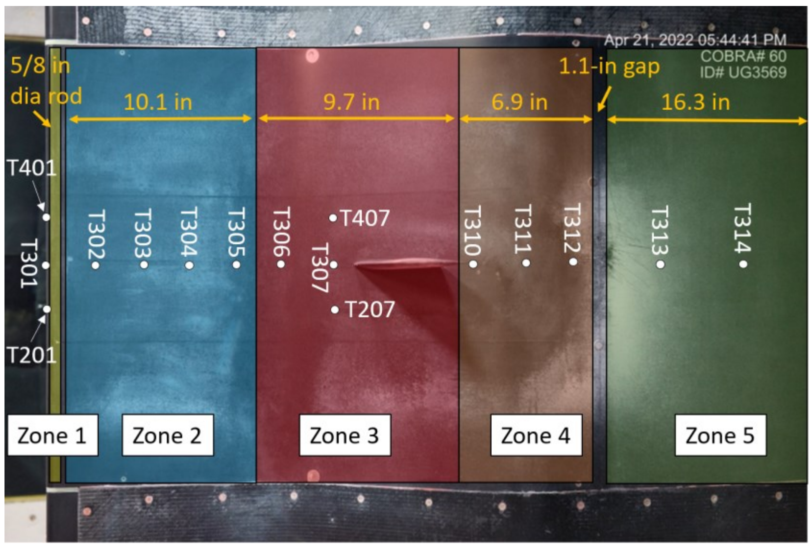

Fig. 9 Image of the SIDRM test article with an overlay of the heater zones approximating the locations they heated, along with the names and locations of several surface mounted thermocouples that are depicted as small white dots.

Resistive heating element gaps exist in each thin film heater. As an example, Fig. 10A shows a schematic of the Zone 3 film heater, where the hatched area represents resistive heating element. A border approximately 0.25 inches wide around each film heater is void of resistive heating element. Thermocouple wire leads pass through holes in the film heaters which resulted in rectangular voids in the resistive heating elements about 0.75 x 1.0 inches in size. The highly conductive aluminum skin (0.25-in thickness) diffuses the heat effectively and heating non-uniformity was considered negligible from these heating element void regions. However, a significant resistive heating element void exists under the strut and can be seen in Fig. 10A. This produced a measurable temperature difference and can be seen in Fig. 10B. Steady state thermocouple temperatures are shown for a test condition prior to spray activation and T307, which is located just upstream of the strut, reads several degrees colder than the other thermocouples in heating Zone 3. The solid aluminum struts, which are unheated, also act as a heat sinks, contributing to the lower temperature reading.

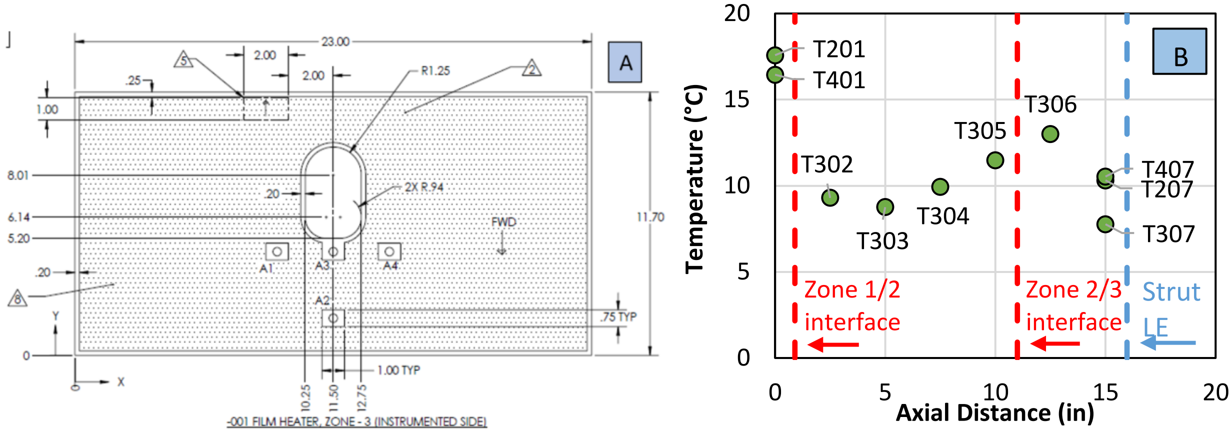

Fig. 10 Figures showing (A) an example of the film heater resistive heating element footprint, and (B) typical surface temperature profile for the forward portion of the test article, where thermocouples nearest the strut, especially T307, show lower temperatures due to the absence of resistive heating element under the strut.

V. Test Procedures

The testing procedures for the ice crystal accretion tests are outlined below. A 4-minute equilibrium spray was performed prior to the first accretion test of the day or after a full tunnel thaw. The equilibrium spray introduced humidity to the flowing air and brought the tunnel to near saturation (100% relative humidity) at the test section. The test article was unheated during the equilibration spray, so ice crystal particles simply bounced off the surfaces. Equilibrium sprays were conducted during the ice crystal cloud characterization tests, so this practice remained constant.

1. Run up IRT to target test airspeed and air temperature.
2. Activate SIDRM heaters to target heat flux values and wait until TCs read steady values.
3. Start recording data 30 seconds prior to spray activation.
4. Turn on IC cloud (spray on).
5. Turn off IC cloud per the time specified on the test matrix (SIDRM heaters turned off simultaneously with spray off).
6. Continue holding tunnel airspeed and air temperature constant as data systems continue recording 30 seconds post spray.
7. Stop data recording systems and shut down drive fan.
8. Enter test section and take photographs of accreted ice.
9. Perform 3D scan of accreted ice.
10. Using heated knife, cut out extents of accreted ice and scrape ice into tray for weighing.
11. Remove all ice from SIDRM and clean test article, preparing for next test point.

Figure 11 shows an ice crystal ice accretion on the SIDRM test article with boxes indicating regions where the 3D laser scan was taken (red box) and ice mass weighed (green box). Hexagon's Romer Absolute SI 7530 scanner was used to scan the ice and has a repeatability accuracy of +/- 0.003". The center 10-in (0.25-m) span was scanned from the leading edge to the extent of ice on either side of the test article. After scanning, the center 8-in (0.20-m) span of accreted ice was carefully cut from the leading edge to the extent of icing on both sides, removed, and weighed.

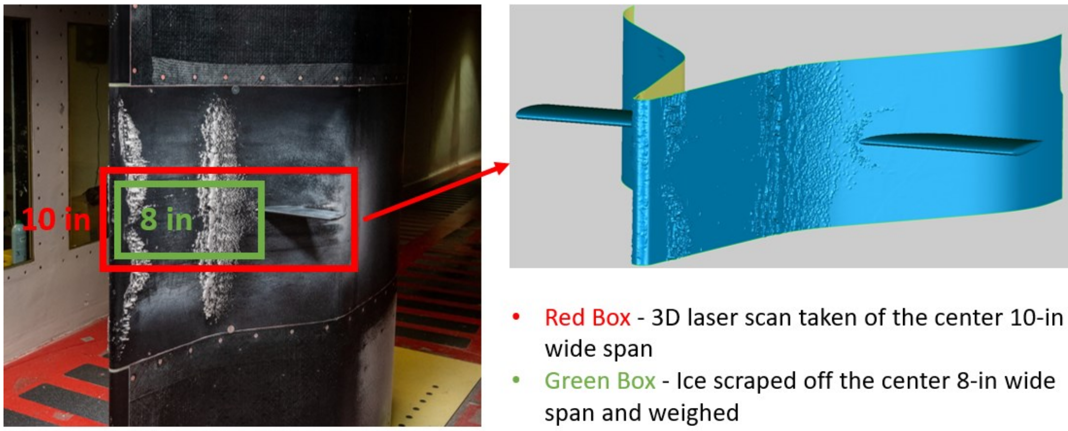

Fig. 11 Ice accretion on the SIDRM test article with boxes indicating regions where the 3D laser scan was taken (red box) and ice mass weighed (green box). The resulting 3D scan is shown on the right.

Ice crystal ice accretions tended to accrete in separate regions on the test article. Figure 12 shows the different regions where ice mass was measured. Figure 12A shows the instrumented side of the test article where ice mass was collected at the ramp base near the strut (South Casing blue box). Figure 12B shows the non-instrumented side of the test article where ice was collected at the ramp base (North Casing red box). Ice mass from near the leading edge was collected and combined from both sides (green boxes in Fig. 12A and 12B). The ice mass was not measured if ice accretions were very small, such as what is shown in the red North Casing box in Fig. 12B.

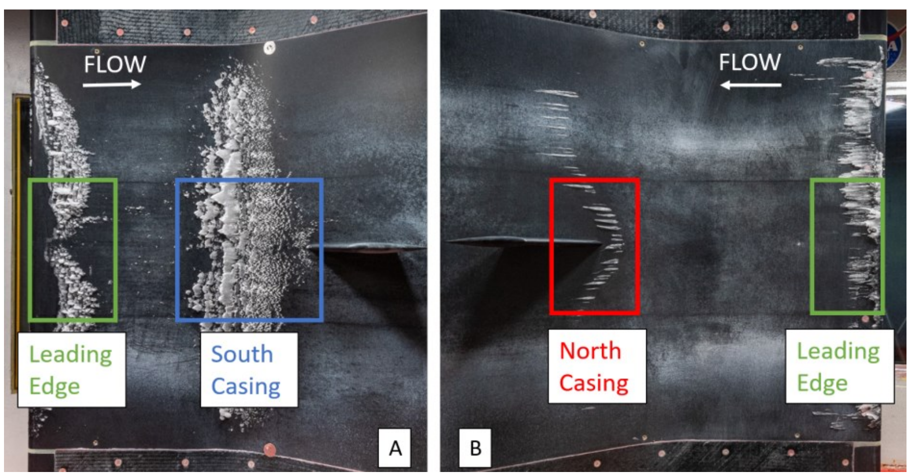

Fig. 12 Images showing the separately weighed regions of accreted ice at the (A) South casing near the strut, (B) the North casing near the strut, and (A & B) near the leading edge which was combined from both sides of the test article.

VI. Ice Crystal Icing Results Using the SIDRM Test Article and Discussion

This test entry represents the first time ice accretions were generated using an ice crystal cloud and test article with heated surfaces. While there were specific test objectives, these tests also had an exploratory nature as this was a first effort of this nature and many unknowns existed, specifically how different heat fluxes will impact icing. The objective for all tests was to generate accretions without shedding ice or limit the amount of shedding. This was desired so the scanning and weighing of the accreted ice at the end of a test run would represent the entire accretion process. Conditions that produced ice but had one or more significant sheds provided less valuable quantitative data. Whereas understanding the conditions that produce continuous build-and-shed accretions is important as well, that was beyond the scope of this effort. The following sections provide key findings and trends related to parameters that impacted ice accretion mass, icing location, and icing characteristics.

A. Icing Accretion Test Condition Matrix

Table 3 shows the target test conditions that were run along with corresponding accreted ice mass. A total of 20 icing tests are presented. The test matrix can be broken into 6 testing blocks.

1. Block 1: Explored the impact of *AOA* and various heater settings on ice accretion conducted at T_0 = -20 °C.
2. Block 2: Explored the impact of *AOA* and various heater settings on ice accretion conducted at T_0 = -15 °C.
3. Block 3: Investigated the contribution of liquid melt from the leading edge by isolating the heaters near the leading edge with downstream zones unheated.
4. Block 4: Explore the minimum flux required at the leading edge to generate liquid melt and observe any ice accretion downstream. These tests started with low heat flux settings and were incremented until melt or icing was observed. The final ice mass and geometry was not measured.
5. Block 5: A single test was run to explore the impact of an icing cloud with larger *MVD* and *IWC* on ice accretion.
6. Block 6: A single test was run to explore the impact of a greater airspeed on ice accretion.

Table 3 Target test conditions, grouped by test objective with corresponding ice mass that was measured. Tests where a significant shed event occurred are indicated with "(sh)" in the Ice Mass columns.

Target Test Conditions													Ice Mass			
Run ID #	Spray Duration min	T_0 °C	*U* knots	*AOA* °	*MVD* µm	*TWC* g/m^3	Zone 1 Heat Flux W/in^2	Zone 2 Heat Flux W/in^2	Zone 3 Heat Flux W/in^2	Zone 4 Heat Flux W/in^2	Zone 5 Heat Flux W/in^2	Zone 6 Heat Flux W/in^2	South Casing g	North Casing g	Leading Edge g	Total g
Various *AOA* and heater settings at T_0 = -20°C																
UG3553	10	-20	150	0	26.3	2.16	8.9	3.7	4.3	4.0	7.5	4.5	32	33		65
UG3554	10	-20	150	0	26.3	2.16	8.9	3.7	5.6	4.0	7.5	4.5	29 (sh)	35 (sh)		64 (sh)
UG3555	10	-20	150	2	26.3	2.16	8.9	3.7	4.3	4.0	7.5	4.5	28 (sh)	3		31 (sh)
UG3557	10	-20	150	2	26.3	2.16	8.9	3.7	3.3	4.0	7.5	4.5	23	10		33
UG3558	10	-20	150	4	26.3	2.16	8.9	3.7	3.3	4.0	7.5	4.5	39 (sh)	2		41 (sh)
UG3559	10	-20	150	4	26.3	2.16	8.9	3.1	3.3	4.0	7.5	4.5	18		14 (sh)	32 (sh)
Various *AOA* and heater settings at T_0 = -15°C																
UG3560	10	-15	150	0	26.6	1.93	7.1	2.8	3.3	3.2	6.0	3.9	30	33		63
UG3561	10	-15	150	2	26.6	1.93	7.1	2.9	2.8	3.2	6.0	3.9	39	11		50
UG3571	10	-15	150	2	26.6	1.93	7.1	2.4	2.5	3.2	6.1	3.9	9		19	28
UG3562	10	-15	150	4	26.6	1.93	7.1	2.4	2.8	3.2	6.0	3.9	23 (sh)		13	36 (sh)
UG3563	10	-15	150	4	26.6	1.93	7.1	2.4	2.5	3.2	6.0	3.9	24		16 (sh)	40 (sh)
UG3568	10	-15	150	4	26.6	1.93	7.1	2.4	2.5	3.2	6.0	3.9	20		25	45
Leading Edge Contribution Investigation																
UG3564	10	-15	150	0	26.6	1.93	9.5	3.6	3.9	0.0	0.0	0.0	67	22 (sh)		89 (sh)
UG3565	10	-15	150	0	26.6	1.93	8.9	3.4	0.0	0.0	0.0	0.0	25	24		49
UG3567	10	-15	150	0	26.6	1.93	14.2	3.9	0.0	0.0	0.0	0.0	20	20		40
UG3574	10	-15	200	4	27.9	1.98	9.9	3.1	0.0	0.0	0.0	0.0	10	19		29
Leading Edge Heat Flux Threshold for Icing Investigation																
UG3568.1	N/A	-15	150	0	26.6	1.93	2.5 - 6.3	2.1 - 2.9	0.0	0.0	0.0	0.0				N/A
UG3575	N/A	-15	200	0	27.9	1.98	3.1 - 14.2	2.9 - 4.6	0.0	0.0	0.0	0.0				N/A
Larger MVD + TWC																
UG3580	10	-20	150	4	31.6	2.28	8.9	3.1	3.4	4.0	7.5	4.5	26		19	45
Faster Airspeed																
UG3573	10	-15	200	4	27.9	1.98	9.9	3.1	3.3	4.3	7.2	5.1	16 (sh)			16 (sh)

Details of the particle size distributions for the clouds used during the SIDRM ice accretion tests are provided in Table A-2 in the Appendix. The particle size distributions are from measurements made during the ice crystal cloud characterization tests. In addition, as-measured test conditions, along with pre-spray and end-of-test temperatures as measured by the surface thermocouples are provided in Table A-3 in the Appendix. The as-measured total air temperatures provided in Table A-3 incorporate the temperature corrections as was measured during the ice crystal cloud characterization tests.

A power supply controller provided power to the six heating zones, where each of the six zones was controlled independently. For Zone 1 that was heated by a cartridge heater, the heat flux values were calculated using the power as measured by the power supply controller divided by the full surface area of a cylinder with a 0.47-in radius, an approximation for the outer mold line geometry of the leading edge. For Zones 2 – 6, heat flux values were calculated using the power as measured by the power supply controller to each zone and divided by the thin film resistive heating element footprint as shown by the hatched area in Figure 10A. All heat generated by the heaters was approximated to be transferred outward toward the outer mold line of the test article, as the side of the heater facing away from the outer mold line as lined with several layers of insulation.

B. General Observations and ICI Characteristics

This section provides some basic observations made during testing. The following discusses icing characteristics, which includes comments on melted runback, accretion features, uniformity, transient behavior, and shedding.

Melting of ice crystals at the heated leading edge was observed. Figure 13A shows a region near the heated leading edge prior to ice crystal cloud activation, and Fig. 13B shows that region 10 s after spray activation, with several melt runback streaks (rivulets) visible in the flat section of Zone 2. These runback liquid streaks confirm that ice crystals impacting the heated leading edge were melting. This runback melt is consistent as runback streaks had been observed in the full-scale engine icing tests conducted at NASA GRC [24, 29, 32]. This liquid runback aids in ice crystals sticking to the surface further downstream where collision efficiency is higher at the ramp base near the strut in Zone 3.

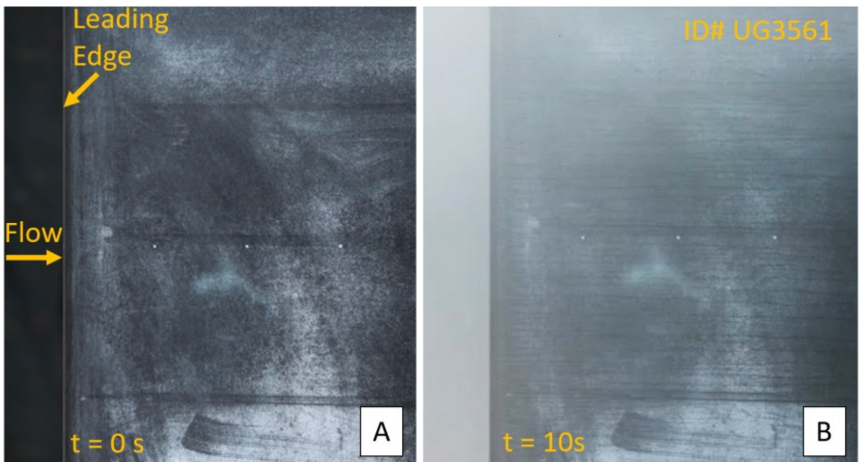

Fig. 13 Images showing the region near the leading edge (a) pre-spray and (b) moments after activation of the ice crystal cloud. The three white dots down the center are the flush-mounted thermocouples. The white marks visible on the surface are paint residue used during the 3D scan process from previous tests.

Figure 14 shows examples of final ice accretions from two test runs that was typical for tests where all heaters (Zones 1 through 6) heated surfaces above 0 °C. The figure serves to illustrate four points. With respect to characterizing the ice accretion at the ramp base near the strut, it was observed that accretions appeared like frozen runback and amorphous in nature as seen in Fig. 14A or contained more orderly “sharkteeth” features as in Fig. 14B. The sharkteeth-like ice accretion features were also observed during the full-scale engine icing tests conducted at NASA GRC [29], suggesting that some basic icing physics were replicated with this component-level test article. Also of note is that for most tests conducted, the strut had little to no impact in terms of a physical anchoring point. During the SIDRM geometry design phase, the location of the strut had been placed just aft of the ramp base with the expectation that it would act as an anchor point for slushy ice that would begin building up at the ramp base, as was observed during other tests. Aside for one test point to be presented later, this was not the case. In addition, the accretions at the ramp base near the strut were observed to be symmetric along the center portion of the span. As was noted during the cloud characterization section, some vertical variation in *IWC* was measured (~±5% in *IWC* for the center 10-in span). For reference, the two darker lines running chordwise in Fig. 14A are marks from the ice cutting knife that span 8 inches apart. A final item to note is that there is evidence that there was some heating non-uniformity from the cartridge heater located at the leading edge. The cartridge heater was designed with a thermocouple located at its center, and that may have impacted heating at the center leading edge. Thermocouple T301 was not working properly during these tests, complicating the issue, but was fixed after testing, confirming thermal non-uniformity near the center at the leading edge. The gap in accreted ice at the center near the leading edge in Figure 14B is likely the result of locally lower heat flux at the leading edge. Despite this non-uniformity, it did not appear to significantly impact the amount of ice accreted at the ramp base near the strut.

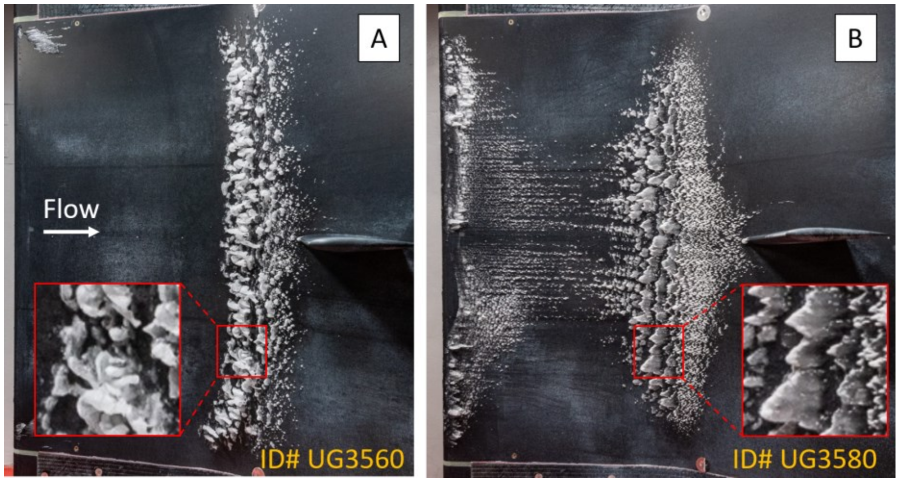

Fig. 14 Images of typical ice crystal ice accretions taken at the end of the test run where ice at the ramp base can be characterized containing (A) amorphous runback streak features, and (B) sharkteeth-like accretion features.

Figure 15 shows ice accretion at 5 moments during the 10-minute test run of run ID# UG3580. The panels show typical transient accretion behavior observed during testing. Accretions began to build up at the ramp base near the strut as seen in Fig. 15A and moved forward with respect to time. For certain test conditions, the accreted ice front moved forward all the way to the leading edge as can be seen in Fig. 15B-E. For most tests, accretion growth ceased or was greatly reduced for a region once ice upstream had accreted.

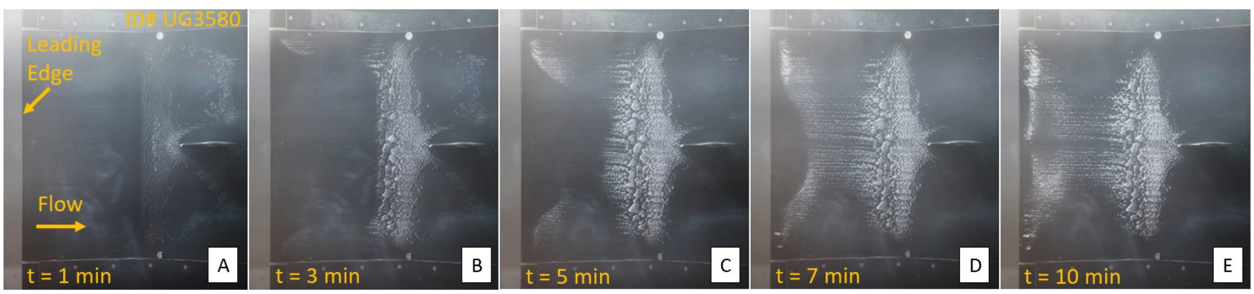

Fig. 15 Images showing typical transient accretion behavior observed during testing.

Figure 16A shows the transient surface temperatures for thermocouples located in the forward half of the test article in heater Zones 1 – 3 for the same test run (ID# UG3580). The figure shows how surface temperature decreased immediately as the ice crystal cloud was activated. Temperatures as measured by thermocouples in Zone 1 and some in Zone 2 appeared to reach momentary steady values reflecting an energy balance between conduction from the heater, convection, melting of ice crystals into runback water, and evaporation/transport downstream of the melted runback. Values continue to decrease to subfreezing temperatures, which coincided with the presence of accreted ice above the respective thermocouple. As can be seen, the order of thermocouples measuring subfreezing temperatures moved from the ramp base near the strut towards the leading edge. Thermocouples at the leading edge remained above freezing throughout the duration of the test as the very leading edge remained ice-free as can be seen in Fig. 15E. Figure 16B shows cross sections of the ice accretion at three span-wise locations at the ramp base near the strut junction on the instrumented side at the end of the 10-minute run from the laser scanned data. The sharkteeth features are represented by the small ridges located around the chord distance Z = -11 inches (the leading edge is at Z = 0 in). This figure shows how the ice crystal accretion was shallow, which was typical of all test runs. Due to the shallow ice accretion geometry, this paper will show photos of the accreted ice as they are much easier to visualize than the cross section from the scans.

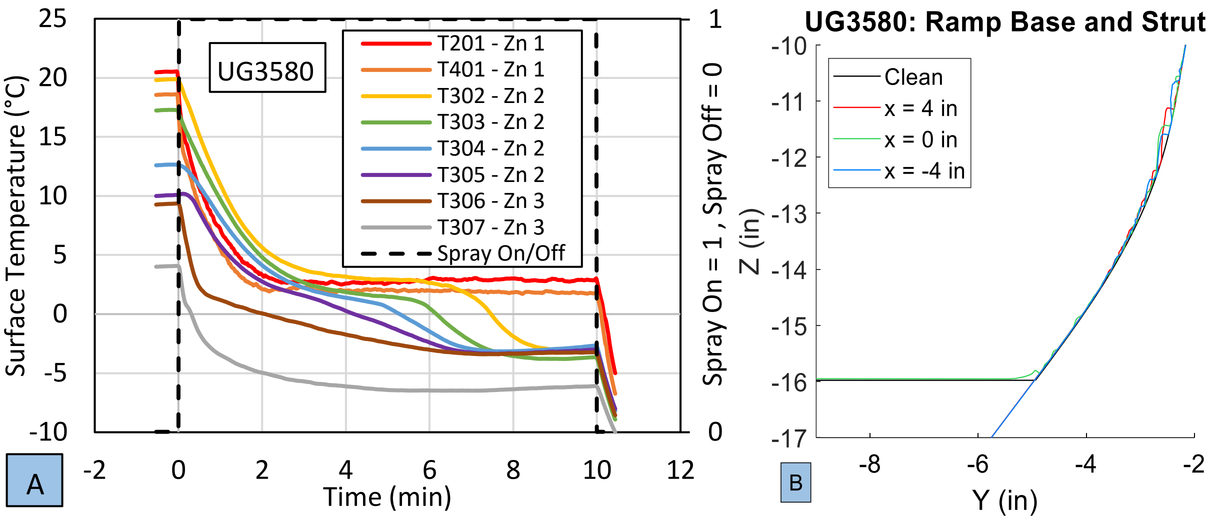

Fig. 16 Graphs showing (A) the transient surface temperatures during an ice crystal accretion test run and (B) the scanned ice accretion at 3 span locations at the ramp base and strut.

As stated earlier, an objective of this study was to accrete ice without shedding so the mass and 3D laser scan of the ice geometry fully represent the ice accretion event. Occasionally small feather-like ice would shed during a test run and was considered negligible in the overall accretion event. However, on occasion a significant shed occurred and was considered impactful on the final ice mass and accretion geometry. As an example, the red boxes in Figs. 17A and 17B show moments before and after a significant partial shed during the middle of a test run. Most tests reported in this paper did not encounter a significant shed event but is noted if one did occur.

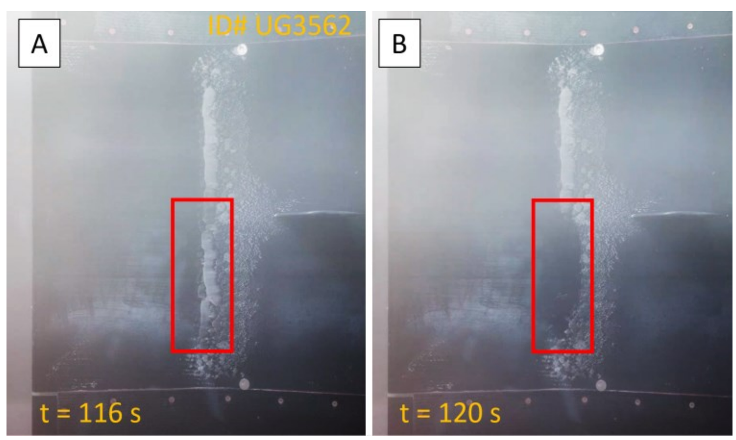

Fig. 17 Images (A) prior to and (B) after a significant partial shed that occurred during an icing test run.

C. Leading Edge Heat Flux Threshold for Icing Investigation

Two tests were dedicated to investigating the minimum heat flux required near the leading edge to produce liquid runback and observe any ice accretion downstream. These tests started with low heat flux settings and were incremented to warmer conditions until melt or icing was observed. Only heating Zones 1 and 2 were activated with the intent of observing liquid runback freezing in the cold unheated zones. The spray was continuous, but the test article was allowed to reach thermal equilibrium before moving on to a new heater setting. The two tests were conducted at airspeeds of 150 and 200 knots to see how airspeed impacted the minimum heat flux threshold required to produce melted runback. Both were run with identical clouds at AOA = 0° and T_0 = -15 °C. Video was viewed to determine when melted runback and icing occurred.

Figure 18A shows an image at the end of the 150-knot icing heat flux threshold test run. A total of 9 heater settings were investigated between Zones 1 and 2. Figure 18B provides the heat flux settings used for Zones 1 and 2, and the corresponding surface temperature as measured by thermocouples in those two zones (Zone abbreviated as "Zn" in Fig. 18B and elsewhere) when the test article reached approximate thermal equilibrium. The initial setting was sufficiently low such that all temperatures were subfreezing, which resulted in no liquid melt as all ice crystals bounced off the surface. The first signs of liquid melt runback (rivulets in Zone 2) occurred at heater setting #4. However, no ice downstream was observed at this setting. It is possible that the small amount of melt that was produced fully evaporated before reaching the unheated subfreezing zones. The first instance of liquid runback accreting as ice was observed near the downstream end of Zone 2 at heater setting #5. A narrow band of runback ice is indicated in Fig. 18A. Also noted in Fig. 18A is a faint secondary band of accreted ice at the ramp base. Evidence suggests that this is melted splash from the leading edge that re-impinged on the subfreezing surface downstream and re-froze. This was first observed at heater setting #5 as well. Warmer heater settings were examined, which added to the amount of ice accreted in the runback and secondary splash ice bands. Of note is how T303, T304, and T305 (all in Zone 2) decreased in temperature starting at heater setting #5, even as the leading edge heat flux was increased (Zone 2 heat flux remained constant). This was due to the amount of melt runback at the leading edge increasing with increasing heat fluxes at the leading edge. This, in turn, cooled the downstream surfaces as the increased melt runback removed more heat via evaporative cooling.

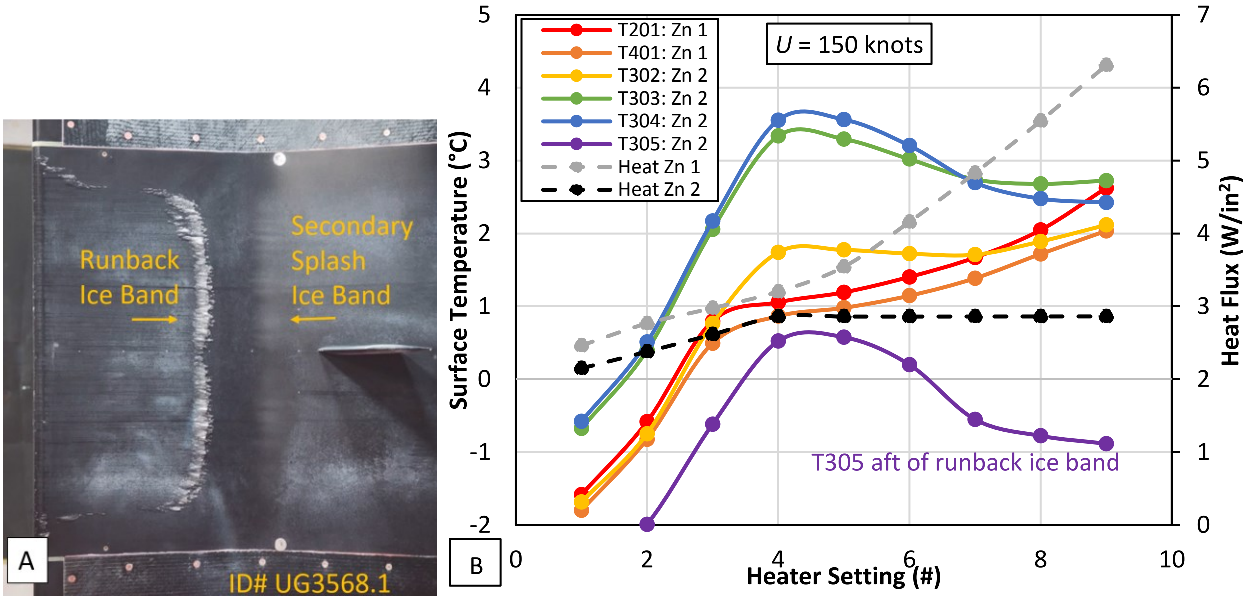

Fig. 18 An image (A) of the accreted ice at the end of the icing heat flux investigation test at 150 knots, and (B) the corresponding Zone 1 and 2 heat fluxes and recorded temperatures at each of the 9 heater settings.

Figure 19A shows an image at the end of the 200-knot icing heat flux threshold test run. Figure 19B provides the heat flux settings used for Zones 1 and 2, and the corresponding steady-state surface temperatures. A total of 14 heater settings were investigated between Zones 1 and 2. The initial setting was sufficiently low such that all thermocouples were near or below freezing and no liquid runback was observed. The first occurrence of melt runback (rivulets in Zone 2), the freezing of liquid runback accreting as ice, and secondary splash accreting downstream all occurred at heater setting #5. The runback ice band and secondary splash ice band are noted in Fig. 19A. Warmer heater settings were examined, which added to the amount of ice accreted in the runback and secondary splash bands. The secondary splash ice band began to grow more prominently starting at heater setting #9. It is important to note that this 200-knot test run explored higher heat flux settings compared to the 150-knot test run and is likely the reason for the more prominent secondary splash ice band. Of note again is how T303, T304, and T305 (all in Zone 2) decreased in temperature when the leading edge heat flux was increased as Zone 2 heat flux remained constant (settings #8, 11, 12, and 13). This reinforces that the amount of melt runback at the leading edge increased with increasing heat fluxes at the leading edge and cooled the downstream surfaces as the increased runback removed more heat via evaporative cooling. It should be noted that some shedding of the runback ice band occurred during testing but did not impact temperature measurements (the ice mass measurement and ice scan were not performed at the end of the test).

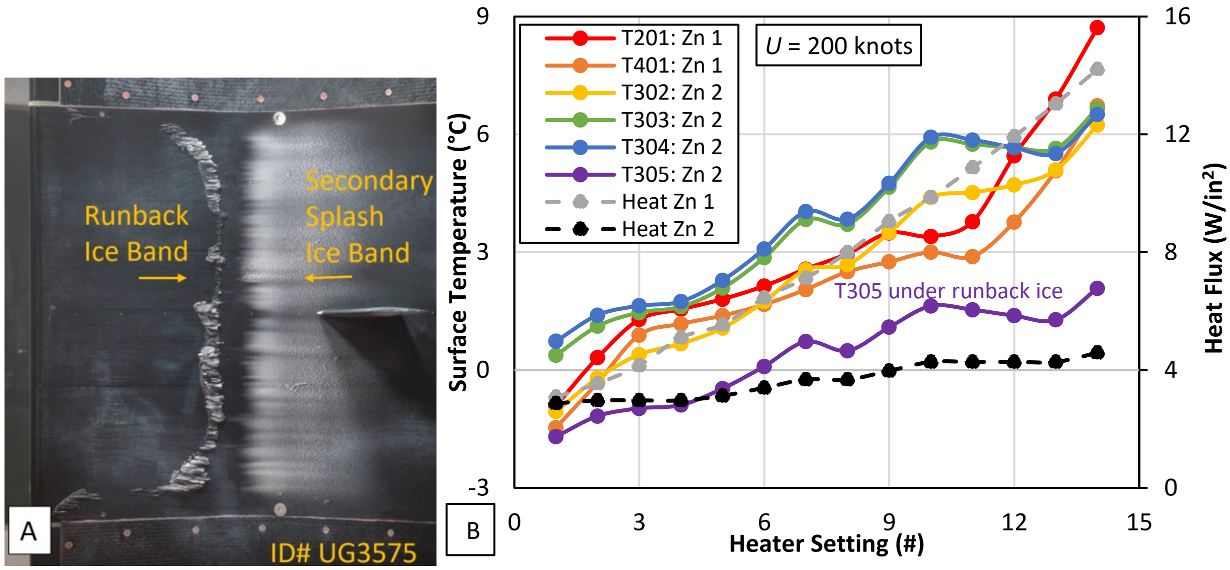

Fig. 19 An image (A) of the accreted ice at the end of the icing heat flux investigation test at 200 knots, and (B) the corresponding Zone 1 and 2 heat fluxes and recorded temperatures at each of the 14 heater settings.

D. Surface Heat Flux Impact on Icing

This sub-section discusses the various impacts surface heat flux settings had on accreted ice mass, location, and characteristics. Four trends are shown from various testing blocks. Images with key conditions and results are shown to demonstrate the impact of heat flux setting.

Figure 20A shows the resulting ice accretion when only Zones 1 and 2 are heated. Figure 20B shows the resulting accretion when Zones 1 through 3 are heated. Both were run under identical cloud conditions at $AOA = 0°$, $T_0 = -15$ °C, and $U = 150$ knots. The heat fluxes in Zones 1 and 2 are slightly higher for the test run with three heated zones but are similar and not expected to have caused the differences in resulting ice accretions. With just heating Zones 1 and 2, similar ice accretion behaviors result as described in the leading edge heat flux icing threshold tests from the previous sub-section. Figure 20A shows the two bands of accreted ice, the runback ice band and secondary splash ice band. This confirms that if heated sufficiently, the leading edge can contribute liquid melt in the form of runback and splash, that eventually re-freeze when they come into contact with subfreezing surfaces farther downstream. The runback ice band acted like an indicator for the 0 °C temperature contour line as the thermocouple that is located under the front edge of the runback ice band measured T305 = 0.4 °C at the end of the test run (T305 = 5.2 °C prior to spray activation). The thermocouple just aft of the runback ice band measured T306 = -7.0 °C at the end of the test run (T305 = 2.9 °C prior to spray activation).

Supplying heat to Zone 3 at the ramp base and strut area significantly changed the resulting ice accretion. Most notably, the location of ice accretion moved farther downstream as the subfreezing surfaces were only measured at the chord location around T307 (compared to chord location around T305 when just Zones 1 and 2 were heated). Lateral conduction losses from Zone 2 into Zone 3 were reduced with the activation of the Zone 3 heater, which increased the downstream surface temperatures of Zone 2. This suggests that by heating Zone 3, the runback remains liquid until it reaches the ramp portion of Zone 3 coinciding with the region where there is an increase in overall collision efficiency, $\beta_{collision}$. The liquid film/rivulets help capture the incoming ice crystals, which increases the collection efficiency, $\beta_{collection}$. The melted splash may be aiding the collection efficiency as well. As a result, the final ice mass was significantly greater with by heating Zone 3.

These tests demonstrate some of the mechanisms of downstream ice accretion with liquid melt from upstream sources. While this heat flux setting and initial thermal profile are not realistic within an engine, it does show how upstream heat sources can supply liquid melt for interaction with impinging particles and eventual ice accretion farther downstream. As had been described in the full-scale engine icing tests conducted with the Honeywell LF11 engine at NASA GRC [29], when upstream heat sources were activated, like the heated spinner or the inlet guide vane anti-ice heat system, additional melt was produced and resulted in quicker rollback, indicating faster (greater) ice growth within the compressor core.

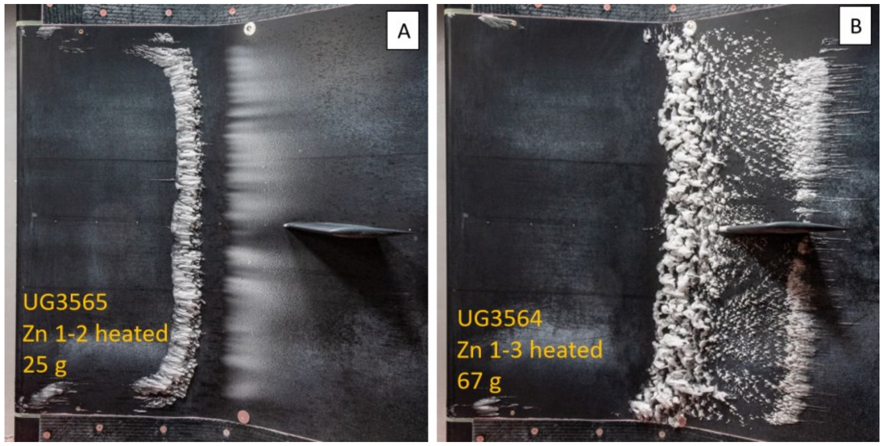

Fig. 20 End of test run images showing (A) the resulting ice accretion when only Zones 1 and 2 are heated and (B) when Zones 1 through 3 are heated.

Figure 21 compares ice accretions between two tests conducted under similar test conditions but with Fig. 21A showing the final ice accretion from a test conducted at a lower heat flux in Zone 3 compared to Fig. 21B. Both were run under identical cloud conditions at AOA = 0°, T_0 = -20 °C, U = 150 knots, and all 6 heated zones had pre-spray surface temperatures above 0 °C. An increase in heat flux at Zone 3 moved the accretion farther downstream for locations away from the strut in lateral (or spanwise) direction. With no heating elements directly under the strut, the locally colder temperatures likely anchored the ice in front of the strut for the test run in Fig. 21B. Meanwhile lateral from the strut, the surfaces were warmer resulting in liquid melt running further downstream until the surfaces became sufficiently cold and froze in Zone 4. The runback streaks at the top of the ramp are noticeable in Fig. 21B. The higher heat flux setting also resulted in multiple ice build and sheds throughout the run in the regions lateral to the strut. This icing behavior can be correlated to behavior observed during the full-scale engine icing tests conducted with the Honeywell LF11 engine at NASA GRC [29]. In that report the authors stated that "increasing N1 (fan speed) can be an effective way to increase the temperature in the core flowpath and suppress accretion," and as a result the engine did not experience any performance rollback. The increase in heat flux in Zone 3 effectively suppressed accretion in Zone 3 lateral to the strut.

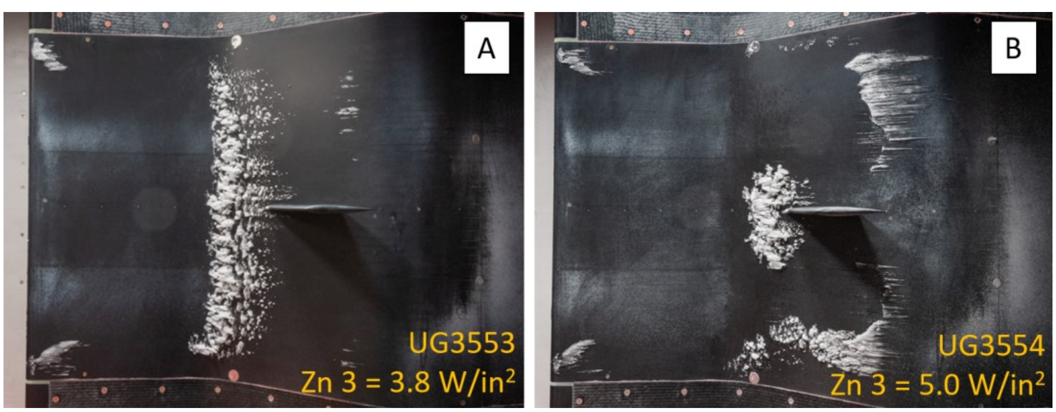

Fig. 21 End of test run images showing (A) the resulting ice accretion for a lower Zone 3 heat flux and (B) how the ice accretion moved downstream at a higher Zone 3 heat flux.

Figure 22 also illustrates the impact of heat flux settings on ice accretion location, with Fig. 22A showing the final ice accretion for a test run with lower heat flux settings in Zones 1 and 2 compared to the test run shown in Fig. 22B. Both were run under identical cloud conditions at AOA = 0°, T_0 = -15 °C and U = 150 knots, with only Zones 1 and 2 heated. With Zones 3 – 6 unheated, this resulted in ice accretion features similar to those discussed in the leading edge heat flux icing threshold tests. Runback icing bands and secondary splash icing bands are visible in both tests. The red circles in Fig. 22 indicate the locations of thermocouples T305 and T306 and provide a reference for the location of the runback ice bands. The runback ice band is slightly farther downstream for the higher heater setting test as the 0 °C surface contour line is farther aft on the test article, the approximate location liquid runback is expected to freeze. Figure 22 shows thermocouple T305 and T306 temperatures at the end of the test run. The 0 °C contour line for Fig. 22A exists approximately at the chord location near thermocouple T305, with that thermocouple reading 0.4 °C and the ice band accreted on top of it. The 0 °C contour line for Fig. 22B exists at a chord location where the runback ice band accreted between thermocouples T305 and T306, with measured temperature values of 4.1 and -4.7 °C, respectively. It is worth noting that the secondary splash ice band location did not change between the two tests. This reinforces the hypothesis that this is melted splash from the leading edge that refroze on subfreezing surfaces further downstream. Since the surface that the melted splash was striking was subfreezing in both test runs, the location of that band was not expected to change.

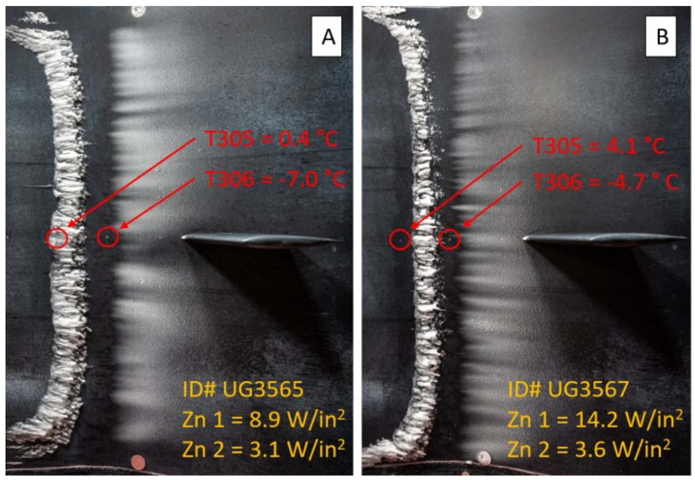

Fig. 22 End of test run images showing ice accretions resulting from tests conducted where Zones 1 and 2 heat flux values were at (A) lower settings and (B) at higher settings. The red circles show the location of two thermocouples as reference to visualize the location of the ice accretions, along with the temperatures measured by the end of the test run.

Figure 23 illustrates the impact of heat flux on accreted ice mass and location with examples provided from two pairs of test runs. For the first pair, Fig. 23A shows ice accretions resulting from a test run conducted at a lower Zone 2 heat flux value, compared to Fig. 23B. Similarly, Fig. 23C shows ice accretions resulting from a test run conducted at lower Zone 2 and 3 heat flux values, compared to Fig. 23D. Greater ice mass was measured at the ramp base for both test runs conducted at higher heat flux settings. The higher heat flux settings kept the region near the leading edge sufficiently warm that it did not freeze, which provided a continues supply of liquid melt to the ramp base throughout the duration of the test runs. The continuous supply of liquid melt at the ramp base likely aided in the capture/sticking of impinging ice particles at this higher collision efficiency area, resulting in greater ice mass accretions. Figures 23A and 23C show how upstream zones accreted with ice limit the supply of runback melt to the ramp base. These test runs reinforce the concept of how upstream heat sources that supply liquid melt to critical regions downstream can lead to larger ice accretions. Again, this is similar to the icing behavior observed during the full-scale engine icing tests conducted with the Honeywell LF11 engine [29] where upstream heat sources provided additional melt, promoting accretion within the compressor core and quicker engine performance rollback.

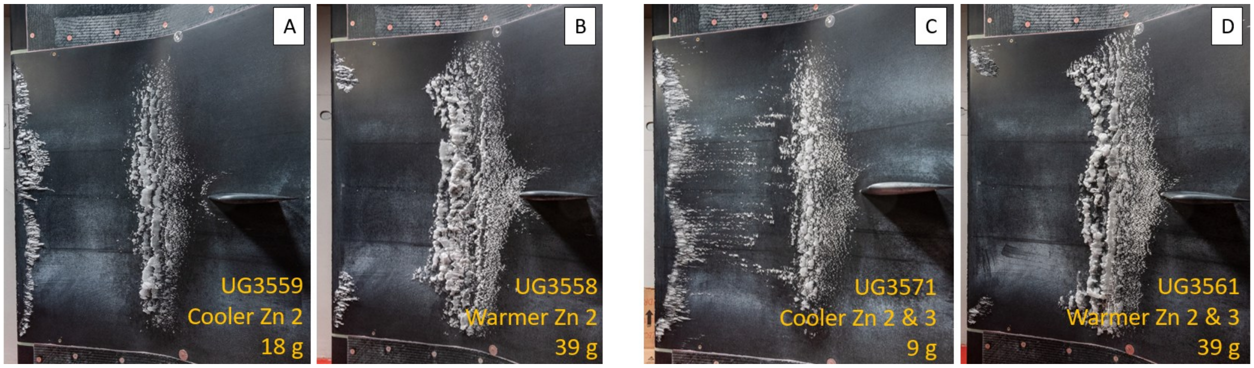

Fig. 23 End of test run images for two pairs of tests. The first pair shows ice accretions resulting from Zone 2 heat flux values at (A) lower settings and (B) at higher settings. The second pair shows ice accretions resulting from Zone 2 and 3 heat flux values at (C) lower settings and (D) at higher settings. Mass measurement from ramp region.

E. Angle of Attack Impact on Icing

This sub-section discusses the impacts angle of attack had on accreted ice mass and icing characteristics. Two trends related to *AOA* were observed. Images with key conditions and results are shown to demonstrate the impact of *AOA*.

Figure 24 illustrates how *AOA* impacted accreted ice mass with examples provided from two pairs of tests. For the first pair that was conducted at T_0 = -15 °C, Figure 24A shows ice accretions resulting from a test run conducted at *AOA* = 2°, whereas Fig. 24B was conducted at *AOA* = 4°. For the second pair that was conducted at T_0 = -20 °C, Figure 24C shows ice accretions resulting from a test run conducted at *AOA* = 2°, whereas Fig. 24D was conducted at *AOA* = 4°. For reference, at positive angles of attack, the leading edge of the model is rotated away from the camera, resulting in the instrumented side becoming the pressure side. Greater ice mass was weighed at the ramp base on the pressure side (the side shown in Fig. 24) for both test runs conducted at larger angles of attack. A higher collision efficiency at the ramp base is expected at larger *AOA*, which was likely a factor in the greater ice mass that was measured. This has implications for designs that have sharper gooseneck angles in the compressor core that can promote higher collision efficiencies.

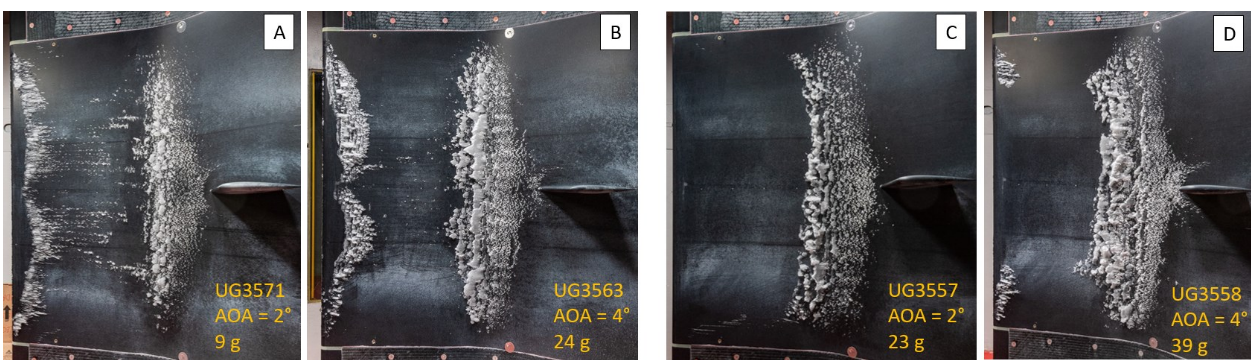

Fig. 24 End of test run images for two pairs of tests. The first pair shows ice accretions resulting from tests conducted at T_0 = -15 °C where (A) *AOA* = 2° and (B) *AOA* = 4°. The second pair shows ice accretions resulting from tests conducted at T_0 = -20 °C where (C) *AOA* = 2° and (D) *AOA* = 4°.

It was observed during testing that ice accretions with sharkteeth features were more prominent at larger angles of attack. Figure 25 shows two pairs of tests and how the larger *AOA* test runs generated more prominent sharkteeth features. No sharkteeth ice features were observed for tests conducted at AOA = 0°, as shown in Fig. 25A, but increasing the angle of attack to 2° for the same test conditions produced some amount of sharkteeth, as shown in Fig. 25B. The second pair shows the same trend. Some sharkteeth ice features can be seen at *AOA* = 2° in Fig. 25C, and more prominent features can be seen for the same test conditions at *AOA* = 4° in Fig. 25D. Interpretations on sharkteeth icing features and icing behavior are provided later in the discussion section.

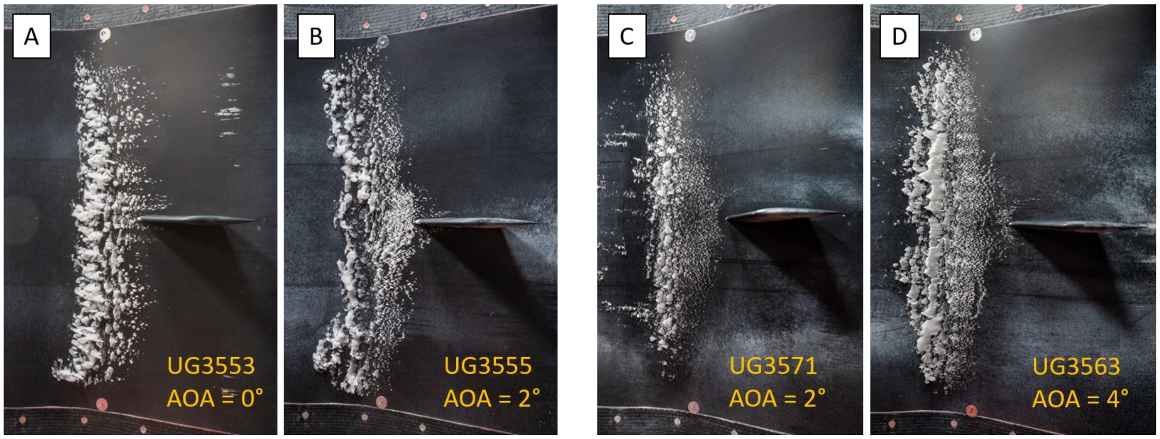

Fig. 25 End of test run images for two pairs of tests. The first pair shows ice accretions resulting from tests conducted at (A) *AOA* = 0° and (B) *AOA* = 2°. The second pair shows ice accretions resulting from tests conducted at (C) *AOA* = 2° and (D) *AOA* = 4°.

F. *MVD* and *TWC* Impact on Icing

Tests were run to examine how cloud *MVD* and *TWC* influenced ice accretion. Figure 26A shows the final ice accretion for a test conducted with smaller *MVD* and *TWC* compared to the test run shown in Fig. 26B. Both were conducted at *AOA* = 4°, T_0 = -15 °C, and *U* = 150 knots, with identical heat flux settings. The initial temperatures as measured by all surface thermocouples were above 0 °C. The differences in cloud *MVD* (32 vs 26 µm) and *TWC* (2.28 vs 2.16 g/m^3) were small but appeared to impact accreted ice mass. A larger total ice mass was measured for the ice cloud with larger *MVD* and *TWC* (45 g vs 32 g). Greater collision efficiency at all locations including the ramp base is expected for clouds with larger *MVD*. Combined with slightly greater *TWC*, these are the likely reasons for the larger accreted ice mass for the cloud with larger *MVD* and *TWC*. Also of note is that the surface temperatures in Zones 2 and 3 at the end of the test run were lower for the run with larger *MVD* and *TWC*. This too may be a result of the higher collision (and collection) efficiency that led to greater cooling with the cloud with larger *MVD* and *TWC*. These final temperature values for these test runs can be seen in Table A-3 in the Appendix.

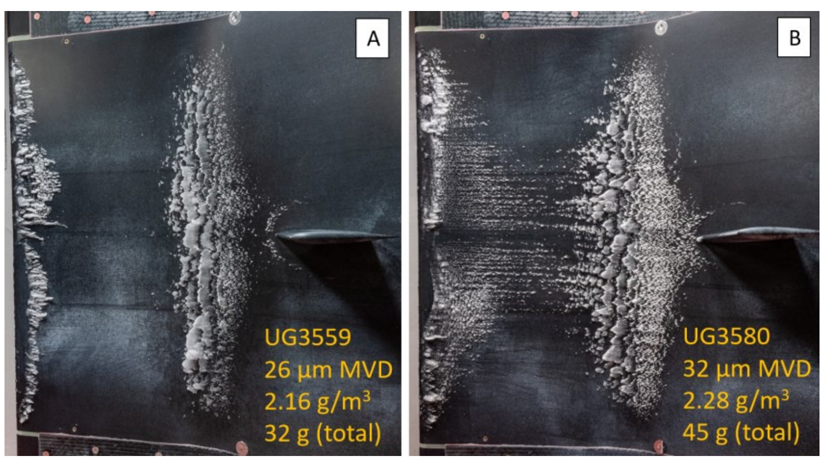

Fig. 26 End of test run images showing ice accretions resulting from tests conducted spraying (A) a smaller *MVD* and *TWC* cloud and (B) spraying a larger *MVD* and *TWC* cloud.

G. Discussion on ice accretion features and behavior

Multiple tests were presented where surface heating was limited to just Zones 1 and 2 to isolate the contribution of liquid melt produced at the leading edge. These tests have shown that ice crystal particles melt when they impact heated surfaces near the leading edge. A greater fraction of the impinging ice crystal cloud at the leading edge melts at higher heater settings. For the test conditions run, evidence suggests that the liquid melt traveled to downstream surfaces by means of runback along the test article surface or as splash that traveled through the air until it re-impinged farther downstream. The amount of melt in terms of runback and splash provides a glimpse into the resulting icing behavior and final ice accretion when Zones 3 to 6 are also activated. Multiple test runs are examined to demonstrate how the melt generated at the leading edge dictates icing behavior downstream.

Figure 27 shows the final ice accretions for similar test conditions that resulted from heating only Zones 1 and 2 in Fig. 27A and heating all 6 zones in Fig. 27B. Both tests were conducted at *U* = 150 knots and *AOA* = 0° under identical cloud conditions. The heat fluxes in Zones 1 and 2 are slightly greater for the test run with only the two heated zones but does not impact the following argument. During testing, the ice mass from the two bands in Fig. 27A were not measured separately (they were weighed together), but 3D laser scans of the accreted ice and visual observation suggests that more melt resulted as runback compared to splash. When heater Zones 3 to 6 were activated, the runback melt traveled farther downstream where it encountered impinging ice crystals cloud particles at the ramp base. The runback dominated melt resulted in an ice accretion with amorphous runback features at the ramp base.

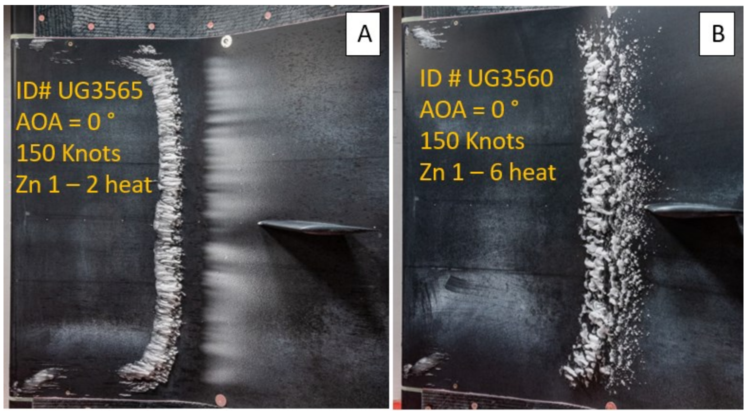

Fig. 27 End of test run images showing ice accretions resulting from tests conducted at *U* = 150 knots and *AOA* = 0° when (A) only Zones 1 and 2 are heated, and (B) when all 6 zones are heated.

The transient ice growth for the test run with all 6 heaters activated (from test run shown in Fig. 27B) reflects an ice accretion at the ramp base where the melt from the leading edge is runback dominated. Figure 28 shows the ice accretion at different times throughout the test run. Focusing on just the region inside the red boxes, Figs. 28A and 28B show that ice accretion moved upstream with respect to time. The ice that initially accreted in the red box at t = 2.5 min. (Fig. 28A) remained approximately the same size as the run progressed, as can be seen in Figs. 28B-D. Instead, ice continued to grow at the front edge of the ice accretion either by moving upstream or growing in greater amounts in the same location as can be seen progressing from Figs. 28A-D. Once a surface upstream accreted with ice, the accreted ice just aft stopped growing or grew a negligible amount. This is characteristic of an accreting ice that is dominated by runback melt.

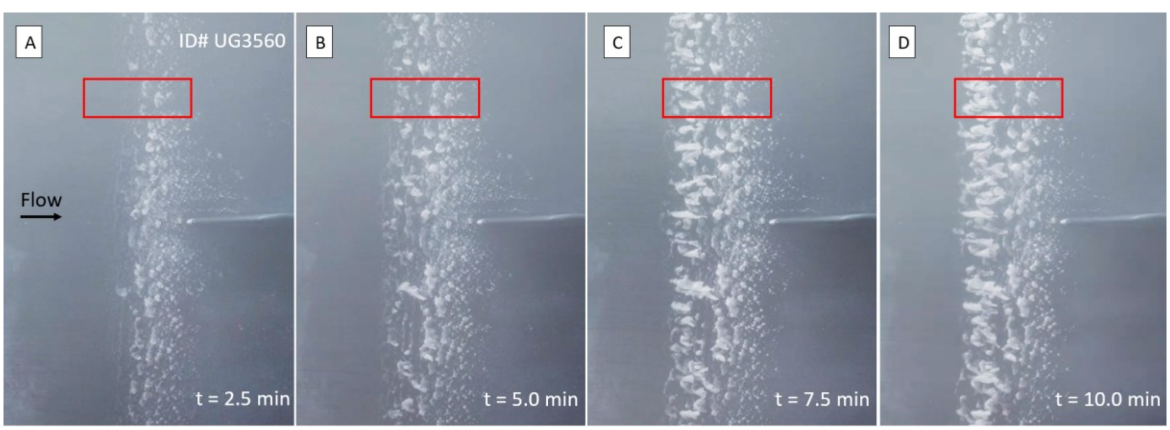

Fig. 28 Images showing the transient progression of ice accretion where the source of melt is runback dominated.

Figure 29 shows the final ice accretions for similar test conditions, that resulted from heating only Zones 1 and 2 in Fig. 29A and heating all 6 zones in Fig. 29B. Both tests were conducted at U = 200 knots and AOA = 4° under identical cloud conditions. The heat fluxes in Zones 1 and 2 were also identical between the two test runs. Figure 29A shows a dominant splash icing band at the base of the ramp indicated by rimy texture. Because the surface at this location was not heated, the splash melt froze immediately on impact, forming rime accretion. Frozen runback streaks were present along the chord of Zone 2. There was no defined runback ice band as has been observed in other test runs that investigated melt contribution from the leading edge. During testing, only the ice mass from the splash band was weighed (the runback streaks were not weighed), but 3D laser scans of the accreted ice and visual observation suggests that more melt resulted as splash compared to runback. There were ice particles from the cloud impacting the base of the ramp where the splash ice formed. However, since there was no liquid on the surface the ice particles most likely bounced off and did not contribute to the ice accretion. When heater Zones 3 – 6 were activated, the warmer surfaces at the ramp base may have kept the splash melt from freezing on contact, helping to collect impinging ice crystal cloud particles. The splash dominant melt resulted in an ice accretion with pointy sharkteeth ice features at the ramp base.

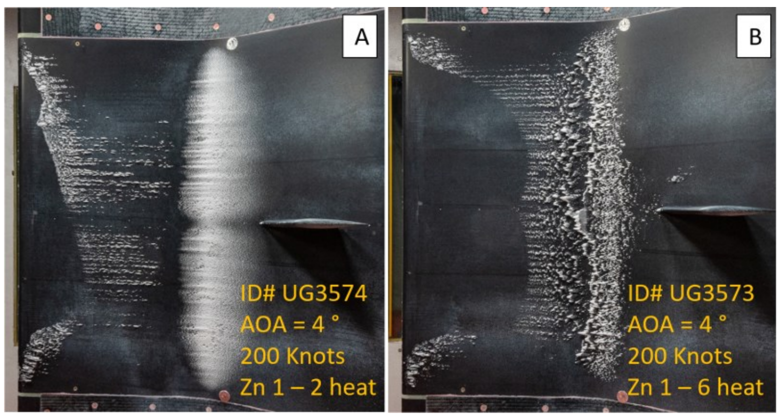

Fig. 29 End of test run images showing ice accretions resulting from tests conducted at *U* = 200 knots and *AOA* = 4° when (A) only Zones 1 and 2 are heated, and (B) when all 6 zones are heated.

The transient ice growth for the test run with all 6 heaters activated (from test run shown in Fig. 29B) reflects an ice accretion at the ramp base where the melt from the leading edge is splash dominant. Figure 30 shows the ice accretion at different times throughout the test run. A significant ice shed occurred just prior to the image in Fig. 30A resulting in the asymmetric accretion towards the front edge of the accretion. Looking at the overall ice accretion, Figs. 30A-D show ice grew forward, indicating the presence of runback melt. The runback froze in streaks in Zone 2 similarly to the test run where only heater Zones 1 and 2 were activated. Focusing on the ramp base, and in particular the region inside the red boxes, despite upstream ice accretion, the sharktooth-shaped ice within the reference red boxes grew throughout the duration of the test. This was the only test run where ice was observed to noticeably grow despite ice accretions upstream. This growth does not appear to be a large amount, but Figs. 30B-D show that all sharkteeth-shaped ice accretions grew longer and pointier throughout the test. Shapes with points will have locally higher collection efficiency, resulting in even pointier ice accretions. This icing behavior falls in line with what can be expected from ice accretions that are dominated by splash melt.

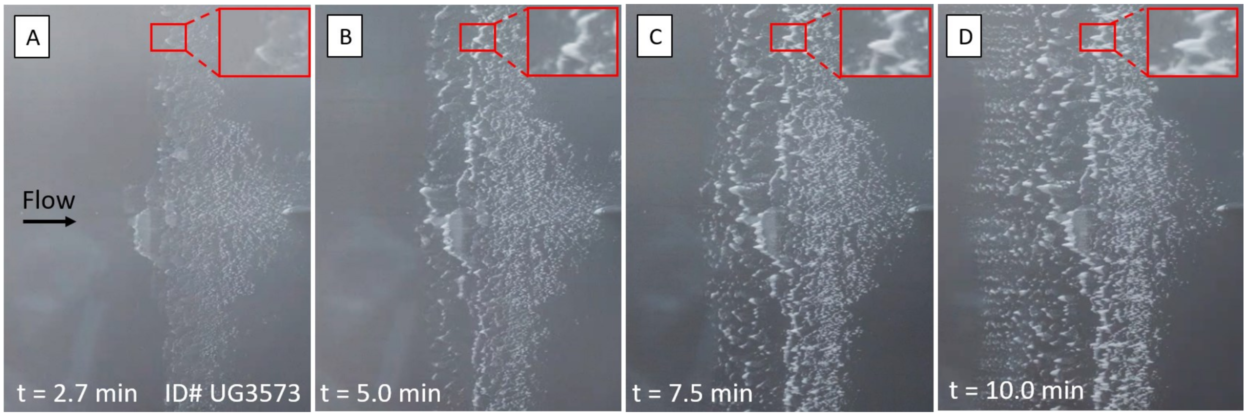

Fig. 30 Images showing the transient progression of ice accretion where the source of melt is splash dominated, and in this case generating sharkteeth-shaped ice.

There were a limited number of tests conducted that investigated the contribution of melt from the leading edge, test runs where only heater Zones 1 and 2 were activated. Most tests where sharkteeth-shaped ice features were observed occurred at U = 150 knots and AOA = 4°. Unfortunately, no tests were conducted investigating how much melt is produced at the leading edge and in what form (runback and splash) at these conditions. Despite the lacking test run data, a closer look at the transient ice accretion at these conditions can provide further insight into sharktooth-shaped ice development and the forms of liquid melt that produced it.

Figure 31 shows ice accretion at different times throughout a test run that resulted in prominent sharkteeth-shaped ice features. The test run was conducted at U = 150 knots and AOA = 4°. Focus is directed to the developing ice within the red boxes. Figure 31A shows a primary icing front whose edge is flat and uniform across the vertical span of the red box. The surface is clear upstream of this primary ice, meaning there is uniform access to runback melt from upstream. Figure 31B shows the primary ice developing into a plateau shape. Small bits of ice can be seen slightly upstream of the primary ice along the upper and lower sides of the red box, corresponding to the valley portion of the plateau shape. These small bits of ice appear to be limiting liquid runback to the primary ice to just the peak of the plateau. Figure 31C shows the primary ice developing pointier features. The small bits of ice upstream and along the red box walls are growing, pinching off the runback melt to the primary ice to a narrower channel. Figure 31D shows the primary ice has fully developed into a sharktooth shape, as ice has accreted upstream across the full vertical span of the red box. This marks 4 minutes into the 10-minute test. Figure 31E shows the accretion after 10 minutes into the spray, and only a small amount of ice growth occurred on the sharktooth-shaped accretion after the 4-minute mark. Since ice had accreted upstream of the primary ice after 4 minutes, only splash melt contributed to this small amount of observed ice growth during this period. Without conducting dedicated test runs to isolate the resulting runback and splash contribution from the leading edge, it is unknown how important splash melt contributed to the overall crystal/liquid mix to develop the sharktooth-shape accretion. However, the transient development described here would suggest that runback melt plays a significant role.

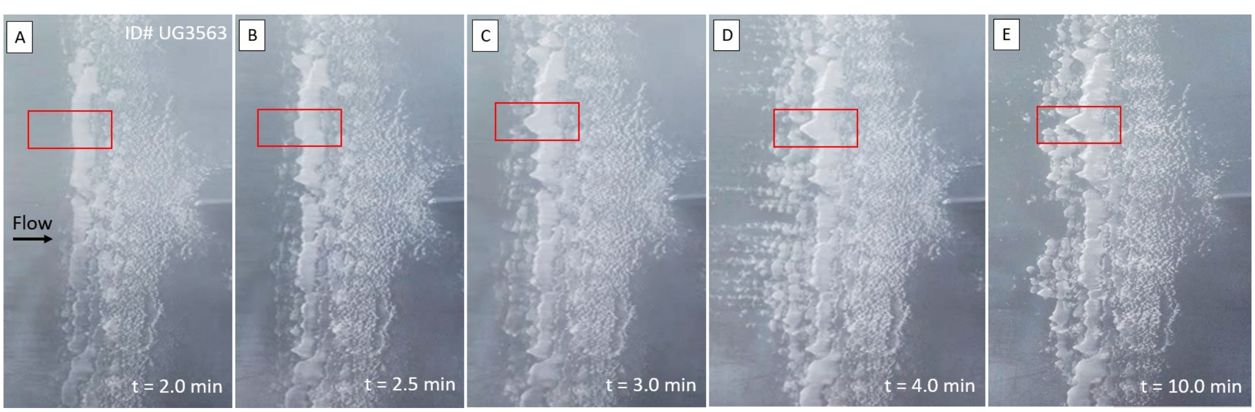

Fig. 31 Images showing the transient progression of sharkteeth-shaped ice accretions.

This subsection described the development of sharkteeth-shaped ice accretions. This was emphasized as sharkteeth-shaped ice accretions had been observed during the full-scale engine icing tests conducted with the Honeywell LF11 engine at NASA [29, 30]. Those ice accretions developed on the outer shroud wall of the transition duct into the high pressure compressor aft of the exit guide vanes. Interpretations of the sharkteeth-shaped ice suggest that it was a result of sharp TWC concentrations on the pressure side of the exit guide vane trailing edge. This may be combined with surface convective heat transfer patterns on the outer shroud wall aft of the exit guide vane that was conducive to accreting the sharktooth-shape. The mechanisms that described the development of sharkteeth-shaped ice accretions during the SIDRM tests appear to be different from those that developed within the LF11 engine. There was no sharp TWC concentration nor known favorable surface convective heat transfer pattern related to the SIDRM icing tests. However, the basic and fundamental elements of liquid and ice crystals coming together on a heated surface are the same for both.

VII. Conclusion

This paper presents results from ice crystal accretion tests utilizing a component level test article with geometry representative of a turbofan inter-compressor. This SIDRM test entry represents the first time that ice accretions were generated using an ice crystal cloud and test article with heated surfaces at the NASA Icing Research Tunnel. This paper also presents results from ice crystal cloud characterization tests that supplemented the accretion tests.

A total of 12 ice crystal cloud test conditions were fully characterized utilizing a wide arrangement of instruments in the test section, most notably measuring *TWC* and the cloud particle size distribution (and in effect *MVD*). The paper discussed the impact of ice crystal cloud recirculation in the closed loop tunnel and its impact on spatial uniformity and *TWC*. Implementing full tunnel thaws at 20 minutes of accumulated spray time helped reduce the impact of particle recirculation by ‘resetting the tunnel’ and providing a means of producing controlled and repeatable ice crystal clouds.

Quantitative data was collected for 20 ice crystal accretion tests presented in this paper. Measurements included test conditions, surface heat flux at 6 heating zones, thermocouple data, heat flux data (not presented here), ice mass, and 3D laser scans of the accreted ice. Various tests were conducted investigating the mechanisms of ice crystal accretion. Accretion tests explored and measured minimum surface heat flux required to melt impinging ice crystals near the leading edge. Tests were run isolating the contribution of liquid melt generated at the leading edge and identified two methods that transported the liquid melt downstream to regions of high collision efficiency: runback and splash. Key trends were identified for various test parameters and how they impacted ice mass, location, and accretion characteristics. Most notably, a sufficiently high surface heat flux at the leading edge (i.e., sufficiently warm) can provide a continuous supply of liquid melt downstream resulting in greater ice mass compared to a lower surface heat flux. A lower flux setting results in the leading edge cooling down enough that it ceases to produce melt for accretion downstream. This can be compared to previously conducted full-scale engine icing tests that observed greater ice growth and reduced engine performance due to heat sources supplying melt downstream to critical areas within the inter-compressor. Larger *MVD* (and *TWC*) clouds, along with greater *AOA* test conditions resulted in greater amounts of ice mass. The greater ice mass result can be directly linked to increased collision efficiency (and collection efficiency) for the larger *MVD* and greater *AOA* test conditions. Another key finding was that higher (warmer) surface heat flux settings in critical accretion zones can suppress ice accretion. This was similarly observed during full-scale engine icing tests where increasing fan speed increased the temperature in the core flowpath and suppressed accretion, improving engine performance where it had encountered engine rollback at slower fan speeds (cooler core flowpath temperature). The paper discussed how runback melt and splash melt from the leading edge impact accretion behavior and characteristics downstream. An in-depth look was taken in identifying some of the mechanisms that generated sharkteeth-shaped ice accretions. The generation of sharkteeth features was of interest as they had been observed in full-scale engine icing tests. However, the mechanisms that generated each appear to be different. While this test entry had exploratory elements, it successfully generated ice accretions on a test article in a fully glaciated cloud, provided a better understanding of some of the icing physics observed, and produced a quantitative dataset for further evaluation for model development and validation.

Appendix

Table A-1 Nominal location of Type-K thermocouples flush with the test article outer mold line. T301 (marked with an asterisk) was not functioning properly during icing tests.

Nominal Location of Surface Mounted Type-K Thermocouples				
TC Name	X (Negative towards floor)	Y (Negative towards instrumented side)	Z (Negative downstream of LE)	Heater Zone
ID	in	in	in	#
T201	-2.500	0.000	0.000	1
T301*	0.000	0.000	0.000	1
T401	2.500	0.000	0.000	1
T302	0.000	-0.842	-2.500	2
T303	0.000	-1.283	-5.000	2
T304	0.000	-1.723	-7.500	2
T305	0.000	-2.164	-10.000	2
T306	0.000	-2.762	-12.500	3
T207	-2.500	-4.196	-15.000	3
T307	0.000	-4.196	-15.000	3
T407	2.500	-4.196	-15.000	3
T310	0.000	-9.207	-21.480	4
T311	0.000	-10.546	-23.980	4
T312	0.000	-10.841	-26.480	4
T313	0.000	-10.830	-31.480	5
T314	0.000	-10.715	-36.480	5
T315	0.000	-7.716	-50.940	6

Table A-2 Particle size distributions of ice crystal clouds presented in this paper, as measured by the Particle Imager – Ice Crystal probe (PI-IC). Mid-point values are provided for each bin.

Cloud MVD →	26.3 µm	26.6 µm	27.9 µm	31.6 µm
Bin Fraction [ ]	Particle Dia [µm]	Particle Dia [µm]	Particle Dia [µm]	Particle Dia [µm]
0.1	5	6	6	6
0.1	12	13	14	14
0.1	16	17	18	19
0.1	20	20	22	23
0.1	24	25	26	29
0.1	29	29	30	35
0.1	34	34	35	42
0.1	41	41	41	50
0.1	50	50	50	64
0.1	71	71	74	100

Table A-3 Measured run conditions with pre-spray and end of icing spray surface thermocouple values.

Measured Run Condition Values																			
Run ID#	UG####	3553	3554	3555	3557	3558	3559	3560	3561	3562	3563	3564	3565	3567	3568	3571	3573	3574	3580
T_0	°C	-20.1	-20.2	-20.2	-20.2	-20.2	-20.1	-15.3	-15.3	-15.4	-15.3	-15.3	-15.3	-15.3	-15.3	-15.3	-15.1	-15.1	-20.0
P_0	psia	14.32	14.32	14.32	14.33	14.33	14.33	14.33	14.33	14.50	14.50	14.50	14.50	14.50	14.41	14.41	14.55	14.55	14.56
U	Knots	149.8	151.0	150.1	150.5	150.3	150.1	149.2	149.6	150.8	150.5	151.2	150.3	149.8	151.6	152.1	199.7	200.8	149.1
AOA	°	0.0	0.0	2.0	2.0	4.0	4.0	0.0	2.0	4.0	4.0	0.0	0.0	0.0	4.0	2.0	4.0	4.0	4.0
MVD	µm	26.3	26.3	26.3	26.3	26.3	26.3	26.6	26.6	26.6	26.6	26.6	26.6	26.6	26.6	26.6	27.9	27.9	31.6
TWC	g/m^3	2.16	2.16	2.16	2.16	2.16	2.16	1.93	1.93	1.93	1.93	1.93	1.93	1.93	1.93	1.93	1.98	1.98	2.28
t	min	10.0	10.0	10.0	10.0	10.0	10.0	10.0	10.0	10.0	10.0	10.0	10.0	10.0	10.0	10.0	10.0	10.0	10.0
Zn 1 Flux	W/in^2	8.9	8.9	8.9	8.9	8.9	8.9	7.1	7.1	7.1	7.1	9.5	8.9	14.2	7.1	7.1	9.9	9.9	8.9
Zn 2 Flux	W/in^2	3.7	3.7	3.7	3.7	3.7	3.1	2.8	2.9	2.4	2.4	3.6	3.4	3.9	2.4	2.4	3.1	3.1	3.1
Zn 3 Flux	W/in^2	4.3	5.6	4.3	3.3	3.3	3.3	3.3	2.8	2.8	2.5	3.9	0.0	0.0	2.5	2.5	3.3	0.0	3.4
Zn 4 Flux	W/in^2	4.0	4.0	4.0	4.0	4.0	4.0	3.2	3.2	3.2	3.2	0.0	0.0	0.0	3.2	3.2	4.3	0.0	4.0
Zn 5 Flux	W/in^2	7.5	7.5	7.5	7.5	7.5	7.5	6.0	6.0	6.0	6.0	0.0	0.0	0.0	6.0	6.1	7.2	0.0	7.5
Zn 6 Flux	W/in^2	4.5	4.5	4.5	4.5	4.5	4.5	3.9	3.9	3.9	3.9	0.0	0.0	0.0	3.9	3.9	5.1	0.0	4.5
Pre-Spray TC values																			
T201	°C	17.6	17.2	19.2	19.6	22.1	20.0	14.5	16.6	16.5	16.6	24.7	20.8	37.6	16.5	15.1	22.4	22.6	20.5
T401	°C	16.4	16.4	18.3	18.4	20.4	18.3	14.0	15.8	15.1	15.3	23.9	19.9	36.6	15.1	14.0	20.5	20.5	18.5
T302	°C	9.3	9.6	13.2	13.7	22.6	18.9	8.4	12.0	15.8	15.7	15.8	12.7	22.5	15.7	9.3	19.9	19.5	19.9
T303	°C	8.8	9.4	11.1	11.1	19.9	15.6	7.9	9.7	13.2	13.0	14.7	11.0	18.0	13.1	6.3	15.3	14.1	17.3
T304	°C	9.9	11.4	11.4	10.7	15.2	11.2	8.8	9.4	9.7	9.4	15.5	9.5	15.3	9.5	5.7	10.9	8.5	12.6
T305	°C	11.5	15.0	12.6	10.5	12.5	9.2	10.1	9.5	8.4	7.8	16.5	5.2	9.7	7.8	5.9	9.3	2.9	10.0
T306	°C	13.0	20.1	14.2	9.7	10.8	8.8	11.6	9.5	8.5	7.5	17.3	-2.9	0.2	7.3	6.2	9.1	-4.6	9.3
T207	°C	10.3	18.0	11.3	6.5	7.1	5.9	9.3	6.9	6.6	5.1	13.8	-8.3	-6.5	5.1	4.1	6.6	-9.3	6.2
T307	°C	7.8	14.7	8.6	4.4	4.9	3.7	7.2	5.0	4.9	3.5	11.3	-8.5	-6.8	3.5	2.5	4.7	-9.6	4.0
T407	°C	10.5	18.1	11.4	6.5	7.1	5.9	9.3	6.8	6.6	5.1	13.9	-8.3	-6.5	5.0	4.1	6.6	-9.5	6.2
T310	°C	1.8	4.9	2.6	0.8	1.4	0.9	2.4	1.8	1.9	1.4	-4.3	-12.6	-11.8	1.3	0.5	2.6	-13.4	1.1
T311	°C	1.6	3.5	2.3	1.3	1.8	1.3	1.9	1.8	2.0	1.6	-8.7	-13.5	-12.9	1.6	0.8	2.9	-14.7	1.5
T312	°C	3.0	4.4	3.6	2.9	3.3	2.8	3.1	3.1	3.2	2.8	-9.6	-13.4	-12.8	3.0	2.2	3.9	-14.4	3.0
T313	°C	18.8	19.9	19.4	18.7	18.9	18.5	16.5	16.3	15.9	15.8	-10.9	-13.4	-12.8	15.7	15.4	15.3	-14.4	18.8
T314	°C	24.0	24.8	24.2	23.6	23.6	23.3	20.6	20.3	19.5	19.5	-11.8	-13.7	-13.1	19.5	19.3	18.3	-14.7	23.4
T315	°C	29.3	30.6	27.0	27.0	24.5	23.8	27.6	25.0	22.6	22.5	-12.7	-13.6	-13.1	22.4	23.7	24.4	-14.6	23.8
End of Spray TC values																			
T201	°C	3.2	3.3	2.8	4.8	3.1	2.6	2.7	2.5	1.7	2.0	5.5	3.3	13.5	2.3	2.6	4.4	3.4	2.9
T401	°C	2.7	2.4	2.2	4.0	2.6	1.8	2.1	2.0	1.4	1.8	5.1	2.8	12.6	1.5	1.9	2.4	2.4	1.8
T302	°C	2.9	2.6	2.9	4.0	2.5	0.3	2.7	2.4	-2.6	0.0	6.1	3.8	10.1	-1.4	0.2	4.4	2.2	-3.2
T303	°C	4.3	4.0	3.6	4.3	2.4	1.0	3.7	2.8	-2.5	0.4	7.4	4.7	9.5	-1.3	-0.1	2.3	-0.7	-3.7
T304	°C	5.5	5.8	4.4	4.6	2.5	1.2	4.5	3.1	-1.4	0.5	8.5	4.5	8.7	-1.0	0.1	0.4	-1.2	-2.7
T305	°C	5.5	7.7	3.6	2.9	1.0	0.1	4.3	1.3	-1.4	-0.5	7.8	0.4	4.1	-1.7	-0.2	-1.2	-3.5	-3.0
T306	°C	2.3	8.0	0.9	-1.4	-1.9	-1.9	1.9	-0.7	-1.6	-1.8	3.1	-7.0	-4.7	-2.6	-1.4	-1.7	-9.0	-3.2
T207	°C	-1.4	2.0	-1.8	-4.6	-4.5	-2.0	-0.8	-3.0	-1.7	-2.7	0.8	-11.3	-9.9	-2.4	-3.1	-1.5	-11.6	-3.7
T307	°C	-3.3	1.0	-3.1	-6.6	-6.6	-4.6	-2.7	-4.6	-3.5	-4.5	-0.8	-11.4	-10.0	-4.2	-4.5	-3.7	-11.8	-6.1
T407	°C	-1.2	2.7	-1.7	-4.6	-4.5	-2.1	-0.8	-3.1	-1.4	-3.1	0.5	-11.2	-10.1	-2.2	-3.0	-2.0	-11.9	-3.6
T310	°C	-1.0	-0.1	-0.4	-2.1	-2.0	-1.1	0.0	-0.8	-0.3	-0.7	-9.3	-13.8	-13.1	-0.7	-0.8	0.6	-13.8	-1.4
T311	°C	-0.7	-0.4	-0.1	-1.2	-1.2	-0.5	0.1	-0.4	0.1	-0.2	-12.1	-14.5	-14.1	-0.1	-0.2	1.3	-14.8	-0.6
T312	°C	1.1	1.4	1.5	0.5	0.5	1.2	1.4	1.0	1.4	1.2	-12.4	-14.2	-13.8	1.4	1.4	2.5	-14.4	1.1
T313	°C	17.9	18.4	18.2	16.9	16.9	17.6	15.4	14.8	14.6	14.7	-12.7	-14.2	-13.6	14.7	15.1	14.6	-14.3	17.7
T314	°C	23.7	24.1	23.5	22.2	22.2	22.8	20.0	19.1	18.7	18.8	-13.0	-14.4	-13.8	18.9	19.3	18.0	-14.4	22.8
T315	°C	25.9	25.8	23.6	22.6	20.7	21.4	25.5	21.7	20.2	19.9	-13.7	-14.2	-14.0	20.0	21.7	25.0	-14.4	22.3

Acknowledgments

The authors would like to thank the many key collaborators without whom this work would not have been possible. Quentin Schwinn and Jordan Salkin of the NASA Imaging Technology Center deserve special thanks for their tremendous work in scanning and processing the ice shape data, in addition to recording and processing the time-lapsed video. We also would like to thank NASA Lead Icing Cloud Characterization Engineer, Emily Timko, for leading test efforts that investigated ice crystal cloud recirculation and spatial uniformity. The authors would also like to acknowledge the staff at the NASA Icing Research Tunnel for their outstanding support as preparing for the test entry and operating the facility in glaciated conditions was a demanding effort. Thank you to intern Emma Nagy from the Georgia Institute of Technology for providing support in analyzing heater measurements. Finally, the authors wish to acknowledge the financial support of the Propulsion Technologies sub-project of the Advanced Air Transport Technology project (AATT) under NASA's Advanced Air Vehicles Program (AAVP).

References

[1] Bravin, M., and Strapp, J.W., "A Continuing Investigation of Diurnal and Location Trends in an Ice Crystal Icing Engine Event Data Base," *SAE International Conference on Icing of Aircraft, Engines, and Structures*, SAE, Minneapolis, MN, 2019, SAE Technical Paper 2019-01-1964.

[2] Bravin, M., Strapp, J.W., and Mason, J., "An Investigation into Location and Convective Lifecycle Trends in an Ice Crystal Icing Engine Event Database," 2015 *SAE International Conference on Icing of Aircraft, Engines, and Structures*, SAE, Prague, Czech Republic, 2015, SAE Technical Paper 2015-01-2130.

[3] Mason, J. G., Strapp, J. W., and Chow, P., "The Ice Particle Threat to Engines in Flight," *44th AIAA Aerospace Sciences Meeting and Exhibit*, AIAA, Reno, NV, 2006, AIAA-2006-206.

[4] Mason, J.G., Chow, P., and Riley, J., "Engine Ice Crystal Icing Technology Plan with Research Needs," Federal Aviation Administration Report, DOT/FAA/TC-20/34, 2020.

[5] Struk, P. M., Agui, J. H., Bartkus, T. P., Tsao, J.-C., King, M. J., and Ratvasky, T. "Ice-Crystal Icing Accretion Studies at the NASA Propulsion Systems Laboratory," *SAE 2019 International Conference on Icing of Aircraft, Engines, and Structures*, SAE, Minneapolis, MN, 2019, SAE Technical Paper 2019-01-1921.

[6] Bartkus, T. P., Tsao, J.-C., and Struk, P. M. "Analysis of Experimental Ice Accretion Data and Assessment of a Thermodynamic Model During Ice Crystal Icing," 2019 *SAE International Conference on Icing of Aircraft, Engines, and Structures*, SAE, Minneapolis, MN, 2019, SAE Technical Paper, 2019-01-2016.

[7] Bartkus, T. P., Struk, P. M., and Tsao, J.-C., "Evaluation of a Thermodynamic Ice Crystal Icing Model Using Experimental Ice Accretion Data", *2018 AIAA Atmospheric and Space Environments Conference*, AIAA, Atlanta, GA, 2018, AIAA-2018-4129.

[8] Struk, P. M., Ratvasky, T. P., Bencic, T., Van Zante, J. F., King, M. C., Tsao, J.-C., and Bartkus, T. P. "An Initial Study of the Fundamentals of Ice Crystal Icing Physics in the NASA Propulsion Systems Laboratory," *9th AIAA Atmospheric and Space Environments Conference*, AIAA, Denver, CO, 2017, AIAA-2017-4242.

[9] Struk, P. M., Tsao, J.-C., and Bartkus, T. B., "Plans and Preliminary Results of Fundamental Studies of Ice Crystal Icing Physics in the NASA Propulsion Systems Laboratory," *8th AIAA Atmospheric and Space Environments Conference*, 2016, AIAA-2016-3738.

[10] Bucknell, A., McGilvray, M., Gillespie, D., Parker, L. et al., "Experimental Study and Analysis of Ice Crystal Accretion on a Gas Turbine Compressor Stator Vane," 2019 *SAE International Conference on Icing of Aircraft, Engines, and Structures*, SAE, Minneapolis, MN, 2019, SAE Technical Paper 2019-01-1927.

[11] Bucknell, A. J., McGilvray, M., Gillespie, D., Jones, G., Reed, A., and Collier, B., "Experimental Studies of Ice Crystal Accretion on an Axisymmetric Body at Engine-Realistic Conditions," *2018 AIAA Atmospheric and Space Environments Conference*, AIAA, Atlanta, GA, 2018, AIAA-2018-4223.

[12] Struk, P. M., King, M. C., Bartkus, T. P., Tsao, J.-C., Fuleki, D., Neuteboom, M., and Chalmers, J. L., "Ice Crystal Icing Physics Study Using a NACA 0012 Airfoil at the National Research Council of Canada's Research Altitude Test Facility," *2018 AIAA Atmospheric and Space Environments Conference*, AIAA, Atlanta, GA, 2018, AIAA-2018-4224.

[13] Struk, P. M., Bartkus, T. P., Tsao, J.-C., Currie, T., and Fuleki, D., "Ice Accretion Measurements on an Airfoil and Wedge in Mixed-Phase Conditions," 2015 *SAE International Conference on Icing of Aircraft, Engines, and Structures*, SAE, Prague, Czech Republic, 2015, SAE Technical Paper 2015-01-2116.

[14] Currie, T. C., Fuleki, D., and Mahallati, A. "Experimental Studies of Mixed-Phase Sticking Efficiency for Ice Crystal Accretion in Jet Engines," *6th AIAA Atmospheric and Space Environments Conference*, AIAA, Atlanta, GA, 2014, AIAA-2014-3049.

[15] Currie, T. C., Fuleki, D., Knezevici, D. C., and MacLeod, J. D. "Altitude Scaling of Ice Crystal Accretion," *5th AIAA Atmospheric and Space Environments Conference*, AIAA, San Diego, 2013, AIAA-2013-2677.

[16] Currie, T. C., Struk, P. M., Tsao, J., Fuleki, D., and Knezevici, D. C. "Fundamental Study of Mixed-Phase Icing with Application to Ice Crystal Accretion in Aircraft Jet Engines," *4th Atmospheric and Space Environments Conference,* AIAA, New Orleans, LA, 2012, AIAA-2012-3035.

[17] Struk, P. M., Broeren, A. P., Tsao, J.-C., Vargas, M., Wright, W. B., Currie, T., Knezevici, D., and Fuleki, D., "Fundamental Ice Crystal Accretion Physics Studies," *SAE 2011 International Conference on Aircraft and Engine Icing and Ground Deicing*, SAE, Chicago, IL, 2011, SAE Technical Paper 2011-38-0018, NASA/TM-2012-217429.
[18] Connolly, J., Choi, M., Yang, X., Doherty, L.J. et al., "Ice Crystal Accretion in a Combined Linear Cascade and Swan Neck Duct," *AIAA AVIATION 2020 FORUM*, AIAA, Virtual Event, 2020, *AIAA-2020*-2828.
[19] Mason, J. G., Chow, P., and Fuleki, D. M., "Understanding Ice Crystal Accretion and Shedding Phenomenon in Jet Engines Using a Rig Test," *Journal of Engineering for Gas Turbines and Power,* Vol. 133, No. 4, 2010, pp. 041201-041201-8. doi: 10.1115/1.4002020.
[20] Mason, J., Neuteboom, M., Chalmers, J., Dumont, C., and Chow, P., "Ice Crystal Environment - Modular Axial Compressor Rig: Comparisons of Ice Accretion for 1 and 2 Stages of Compression," *2023 SAE International Conference on Icing of Aircraft, Engines, and Structures,* SAE, Vienna, Austria, 2023, SAE Technical Paper 2023-01-1397, 2023.
[21] Neuteboom, M., Dumont, C., Mason, J., Chalmers, J., and Chow, P., "NRC's ICE-MACR 2018-2023: What Has Been Learned So Far," *2023 SAE International Conference on Icing of Aircraft, Engines, and Structures,* SAE, Vienna, Austria, 2023, SAE Technical Paper 2023-01-1377.
[22] Neuteboom, M.O. and Chalmers, J.L.Y., "Ice Crystal Environment-Modular Axial Compressor Rig: Transient Analysis of Icing Severity Levels," *AIAA AVIATION 2021 FORUM,* AIAA, Virtual Event, 2021, AIAA-2021-2660.
[23] Neuteboom, M.O., Chalmers, J.L.Y., and Davison, C.R., "Ice Crystal Environment-Modular Axial Compressor Rig: Overview of Altitude Icing Commissioning," *AIAA AVIATION 2020 FORUM*, AIAA, Virtual Event, 2020, AIAA-2020-2823.
[24] Flegel, A. B., "Ice Crystal Icing Investigation on a Honeywell Uncertified Research Engine in an Altitude Simulation Icing Facility," *Proceedings of the ASME Turbo Expo 2020*, London, England, 2020, GT2020-14714.
[25] Tsao, J.-C., "Scaling Evaluation of Ice-Crystal Icing on a Modern Turbofan Engine in PSL Using the COMDES-MELT Code," *SAE International Conference on Icing of Aircraft, Engines, and Structures*, SAE, Minneapolis, MN, 2019, SAE Technical Paper 2019-01-1920.
[26] Rigby, D. L., Wright, W. B., "Numerical Investigation of Particle Breakup and Ingestion into an Axial Low Pressure Compressor at Engine Icing Operating Points," *2018 AIAA Atmospheric and Space Environments Conference*, AIAA, Atlanta, GA, 2018, AIAA-2018-4131.
[27] Tsao, J.-C., "Preliminary Evaluation of Altitude Scaling for Turbofan Engine Ice Crystal Icing," *9th AIAA Atmospheric and Space Environments Conference*, AIAA, Denver, CO, 2017, AIAA-2017-4086.
[28] Rigby, D. L., Ameri, A. A., Veres, J., Jorgenson, P. C. E., "Viscous Three-Dimensional Simulation of Flow in an Axial Low Pressure Compressor at Engine Icing Operating Points," *9th AIAA Atmospheric and Space Environments Conference*, AIAA, Denver, CO, 2017, AIAA-2017-4087.
[29] Flegel, A. B., and Oliver, M. J., "Preliminary Results from a Heavily Instrumented Engine Ice Crystal Icing Test in a Ground Based Altitude Test Facility," *8th AIAA Atmospheric and Space Environments Conference*, 2016, AIAA-2016-3894.
[30] NASA Glenn Research Center, "When Hot Engines meet Ice Clouds" YouTube video [online May 5, 2016], URL: https://www.youtube.com/watch?v=L_6HxvwHsdg.
[31] Veres, J. P., Jorgenson, P. C. E., Jones, S. M., "Modeling of Highly Instrumented Honeywell Turbofan Engine Tested with Ice Crystal Ingestion in the NASA Propulsion System Laboratory," *8th AIAA Atmospheric and Space Environments Conference*, AIAA, Washington D.C., 2016, AIAA-2016-3895.
[32] Oliver, M. J., "Validation Ice Crystal Icing Engine Test in the Propulsion Systems Laboratory at NASA Glenn Research Center," *6th AIAA Atmospheric and Space Environments Conference*, AIAA, Atlanta, GA, 2014, AIAA-2014-2898.
[33] Veres, J. P., Jorgenson, P. C. E., Coennen, R., "Modeling of Commercial Turbofan Engine with Ice Crystal Ingestion; Follow On," *6th AIAA Atmospheric and Space Environments Conference*, AIAA, Atlanta, GA, 2014, AIAA-2014-2899.
[34] Tsao, J.-C., Struk, P, Oliver, M., "Possible Mechanisms for Turbofan Engine Ice Crystal Icing at High Altitude," *6th AIAA Atmospheric and Space Environments Conference*, AIAA, Atlanta, GA, 2014, AIAA-2014-3044.
[35] Bartkus, T., Lee, S., and Stewart, E., "Icing Physics Studies Using the 3D SIDRM Test Article: Aerodynamic and Supercooled Liquid Icing Analysis," *2023 SAE International Conference on Icing of Aircraft, Engines, and Structures,* SAE, Vienna, Austria, 2023, SAE Technical Paper 2023-01-1399.
[36] Stewart, E. and Bartkus, T., "Computational Icing Analysis on NASA's SIDRM Geometry to Investigate Collection Efficiency," *2023 SAE International Conference on Icing of Aircraft, Engines, and Structures,* SAE, Vienna, Austria, 2023, SAE Technical Paper 2023-01-1476.
[37] Bartkus, T. P., Lee, S., Potapczuk, M. G., and Flack. C. A., "Description of Cloud Characterization and Icing Tests for a 3D Heated Test Article at the NASA Icing Research Tunnel," *AIAA AVIATION 2022 FORUM,* AIAA, Chicago, IL, 2022, AIAA-2022-3700.
[38] Bartkus, T., Potapczuk, M., Lee, S., Stewart, E., and Chen, R.-C., "Plans for Ice Crystal Icing Tests Using a 3D Heated Test Article at the NASA Icing Research Tunnel," *AIAA AVIATION 2021 FORUM,* AIAA, Virtual Event, 2021, Oral Presentation.
[39] Porter, C., Potapczuk, M., Ozoroski, T., Sabri, Z, Galloway, E., Rigby, D., Wright, W., and Tsao P., "GlennICE Manual 4.1.0," NASA Technical Memorandum, 2024, NASA/TM-20240002191.
[40] Porter, C.E., "Utilization of Streamtubes to Analyze the Physical Interaction of a Dispersed Cloud with the CRM65 Hybrid Midspan Model," *AIAA AVIATION 2024 FORUM,* AIAA, Las Vegas, NV, 2024, (submitted for publication).
[41] Sabri, Z.H., and Porter, C.E., "A Study of Parallel Scalability and Dynamic Workload Balancing in GlennICE," *AIAA AVIATION 2024 FORUM,* AIAA, Las Vegas, NV, 2024, (submitted for publication).

[42] Sabri, Z. and Porter, C., "Scalability of GlennICE in a Parallel Environment," *2023 SAE International Conference on Icing of Aircraft, Engines, and Structures,* SAE, Vienna, Austria, 2023, SAE Technical Paper 2023-01-1482.
[43] Rigby, D. and von Hardenberg, P., "Demonstration of Initial GlennICE Relative Frame Capability: Axial-Flow Propeller," *2023 SAE International Conference on Icing of Aircraft, Engines, and Structures,* SAE, Vienna, Austria, 2023, SAE Technical Paper 2023-01-1457.
[44] Wright, W., Rigby, D., and Ozoroski, T., "Roughness Parameter Optimization of the McClain Model in GlennICE," *2023 SAE International Conference on Icing of Aircraft, Engines, and Structures,* SAE, Vienna, Austria, 2023, SAE Technical Paper 2023-01-1468.
[45] Wright, W. B., Porter, C. E., Galloway E. T., and Rigby D. L, "GlennICE 2.1 Capabilities and Results," *AIAA AVIATION 2022 FORUM,* AIAA, Chicago, IL, 2022, AIAA-2022-3309.
[46] Porter, C. E., "A Comparison of Trajectory Refinement Schemes for GlennICE," *AIAA AVIATION 2022 FORUM,* AIAA, Chicago, IL, 2022, AIAA-2022-3692.
[47] Wright, W., Porter, C., Galloway, E., and Rigby, D. "An Automated Refinement Process for Particle Trajectory Methods in GlennICE," *AIAA AVIATION 2021 FORUM,* AIAA, Virtual Event, 2021, AIAA-2021-2631.
[48] Porter, C. E., Rigby, D. L., "Three Dimensional Surface Redefinition Method for Computational Ice Accretion Solvers," *AIAA AVIATION 2020 FORUM*, AIAA, Virtual Event, 2020, *AIAA-2020*-2831.
[49] Bartkus, T. P., Struk, P. M., and Tsao, J.-C., "Comparisons of Mixed-Phase Icing Cloud Simulations with Experiments Conducted at the NASA Propulsion Systems Laboratory," *9th AIAA Atmospheric and Space Environments Conference*, AIAA, Denver, CO, 2017, AIAA-2017-4243.
[50] Bartkus, T. P., Struk, P. M., Tsao, J.-C., and Van Zante, J. F., "Numerical Analysis of Mixed-Phase Icing Cloud Simulations in the NASA Propulsion Systems Laboratory," *8th AIAA Atmospheric and Space Environments Conference*, AIAA, Washington D.C., 2016, AIAA-2016-3739.
[51] Bartkus, T. P., Struk, P. M., and Tsao, J.-C., "Development of a Coupled Air and Particle Thermal Model for Engine Icing Test Facilities," *SAE International Journal of Aerospace,* Vol. 8, No. 1, 2015, pp. 15-32, SAE Journal Paper 2015-01-2155.
[52] Clark, C., "Altitude Icing Wind Tunnel Ice Crystal Calibration Report," National Research Council of Canada Report LTR-AL-2022-0105.
[53] Clark, C., Orchard, D., "NRC Altitude Icing Wind Tunnel Ice Crystal Calibration Report," National Research Council of Canada Report LTR-AL-2017-0051.
[54] Lilie, L., Emery, E., Strapp, J. W., and Emery, J. "A Multiwire Hot-Wire Device for Measurement of Icing Severity, Total Water Content, Liquid Water Content, and Droplet Diameter," *43rd AIAA Aerospace Sciences Meeting and Exhibit*, AIAA, Reno, NV, 2005, AIAA-2005-859.